to linear regression analysis.

4.2.5 Lattice parameters

The lattice parameter values are necessary for the interpretation of dilatometric data. The procedure outlined in section 2.4 was adopted. The extrapolation procedure to obtain the lattice parameter is shown in Fig. 4.4. The ferrite lattice parameter was found to be $2.8679 \pm 0.106 \times 10^{-2}$ Å. The predicted lattice parameter using the relations given by Leslie (1982) and Wever (1928) and using a program which again takes into consideration the equilibrium dissolved carbon in ferrite, (Bhadeshia *et al.*, 1990) the lattice parameter of ferrite was calculated and found to be 2.8679 Å, which is in remarkable agreement with the experimental value. The equation for predicting the ferrite lattice parameter is as given below.

$$\begin{aligned} \bar{a}_\alpha = a^\circ_{Fe} + (e_c) - (3.0 \times 10^{-12})M_{Si} + (6.0 \times 10^{-12})M_{Mn} \\ +(7.0 \times 10^{-12})M_{Ni} + (0.31 \times 10^{-10})M_{Mo} \\ +(5.0 \times 10^{-12})M_{Cr} + (0.096 \times 10^{-10})M_V \end{aligned} \quad (4.1)$$

where $M_{Si,Mn,Ni,Mo,Cr,V}$ are mole fractions of alloying elements. a°_{Fe} is the lattice parameter of pure iron taken to be 2.8664 Å, e_c is the expansion in lattice parameter due to carbon dissolved in the ferrite.

4.2.6 Microscopy

The microstructures were observed using optical microscope, scanning electron microscope (SEM) and transmission electron microscope (TEM). The specimen preparation techniques were outlined before (see chapter 2). Some of the selected samples were analysed by energy dispersive X-ray analysis in SEM and in TEM. The prior austenite grain size was measured by thermal grooving and hardness tests were carried out on the heat treated samples.

4.3 Results

4.3.1 Effect of allotriomorphic ferrite

The microstructures obtained in samples F3-5 and corresponding transmission electron micrographs of selected specimens are shown in Fig. 4.5. The microstructures obtained in samples F6-8 and a transmission electron micrograph of sample F6 are shown in Fig. 4.6

The optical microstructure of specimen F3 revealed classic bainite sheaves, consisting of aggregates of small parallel plates, a result confirmed using transmission electron microscopy (Fig. 4.5d & e); this was the expected result, *i.e.*, all platelets within a sheaf have identical crystallographic orientation (Bhadeshia and Edmonds 1979, 1980). This is consistent with the fact

that the sample had been transformed directly to bainite without the intervening isothermal hold at T_1, which would have caused the formation of allotriomorphic ferrite; thus the bainite sheaves nucleate at the undecorated austenite grain boundaries. In contrast, samples F4 and F5 which had been given a two-stage heat treatment, showed very different final microstructure, consisting of layers of allotriomorphic ferrite and intragranularly nucleated acicular ferrite (Fig. 4.5b,c & f). The allotriomorphic ferrite destroys the original austenite grain boundary nucleation sites and thereby forces heterogeneous nucleation of acicular ferrite on intragranular inclusions.

To demonstrate that such drastic changes in microstructure cannot be explained by austenite grain size variations in the present studies, the austenite grain sizes of specimens F5 and F6 were measured and found to be 70 $\pm$ 10 μm for F5 and 76 $\pm$ 11 μm for F6. As expected, the measurements are identical within the limits of the experimental error. The apparent thickness of allotriomorphic ferrite of about 5-10 μm when compared with the austenite grain size shows that, for most of the cases studied, there is sufficient austenite remaining for further transformation at T_2, a condition essential for the intragranular formation of acicular ferrite.

Further experiments were carried out to confirm that acicular ferrite does not form in this alloy unless the transformation temperature T_2 is less than B_S. Specimen F7 was first transformed partially to a similar amount of allotriomorphic ferrite at T_1= 800 °C in the usual way and was then quenched to a higher value of T_2= 600 °C which is above B_S. The microstructure obtained (Fig. 4.6c) shows clearly that transformation above B_S leads simply to the formation of more allotriomorphic ferrite, while any small amount of untransformed austenite decomposes martensitically on cooling to ambient temperature. The microstructure consists essentially of equiaxed allotriomorphic ferrite and small islands of martensite which would have formed on quenching after the second isothermal heat treatment. The results were confirmed further by sample F8, (Fig. 4.6d) which was quenched without any second isothermal heat treatment; allotriomorphic ferrite is again observed as for F7 (or F4,5) but its volume fraction is found to be lower than in F7 due to the absence of the isothermal reaction at 600 °C. The residual austenite has again transformed into martensite instead of acicular ferrite. The result supports the concept that the acicular ferrite microstructure does not form by transformation above B_s.

The volume fractions of allotriomorphic ferrite in samples F4 and F5 were measured to be 0.33 and 0.46, respectively. The calculated equilibrium volume fraction of allotriomorphic ferrite, that can form at 800 °C was found to be 0.20, based on application of the lever rule to the paraequilibrium phase diagram. The thickness of allotriomorphic ferrite that can grow, assuming paraequilibrium carbon diffusion controlled growth, at a given temperature can be

calculated using the following equation (Bhadeshia *et al.*, 1985):

$$q = \alpha_1 \times t^{0.5} \tag{4.2}$$

where q is the half thickness of allotriomorphic ferrite, α_1 is one-dimensional parabolic thickness of ferrite thickness of ferrite and t is the time in seconds.

The calculation using the above equation indicates that, for a holding time of 10 minutes after the initiation of allotriomorphic growth, the thickness of ferrite should be around 6.42 μm . As seen in the Table 4.3, the time needed for a detectable amount of transformation is much higher relative to the time at T_1. Thus, some of the ferrite might have formed while cooling from 800 °C to T_2. Therefore, it is not possible to control the allotriomorphic ferrite reaction because of the low hardenability used. However, this does not affect the concept of the experiment, providing that the amount of allotriomorphic ferrite that forms before bainite reaction is not excessive. The fact that the allotriomorphic ferrite forms during continuous cooling within the range T_1-T_2 is of no consequence, as demonstrated by sample F6, which was cooled continuously from the austenite phase field by keeping the specimen within a sealed quartz tube and holding it in an ice water mixture. This yielded a microstructure in which the austenite grain surfaces were decorated by thin layers of allotriomorphic ferrite layer and acicular ferrite (Fig. 4.6a and 4.6b). The similarity of the microstructure to that observed in the as deposited layers of ordinary C-Mn welds is considerable. The result emphasises the destruction of austenite grain boundary nucleation sites by allotriomorphic ferrite and shows its indirect effect in promoting the transformation of the remaining austenite to acicular ferrite.

EDX analysis (samples F6 and F5 in TEM and SEM, respectively) revealed no discernible change in the bulk substitutional alloying element concentration during allotriomorphic ferrite growth (See Table 4.5) within the experimental error. The areas which were subjected to EDX analysis in TEM and SEM are shown in Fig. 4.7. The figure also shows the variation of Cr, Mn and Si across the allotriomorphic ferrite. This indicates that the allotriomorphic ferrite has inherited the original substitutional alloying element concentration, consistent with a paraequilibrium growth mechanism (see section 1.2.3). The carbon extraction replicas have failed to show any presence of carbides in the transformed samples. This supports the assumption, made in deriving the relation between the length change and volume fraction of ferrite transformed (equation 2.1), that the transformation to bainite is associated with no precipitation of carbides. The replicas were found to contain only inclusions (as the samples were originally taken from weld metal portion) of complex manganese, silicon oxides Table 4.5 also gives a summary of EDX analysis on inclusions in the sample F5.

Table 4.5 Results of microanalysis tests on allotriomorphic-acicular ferrite regions and inclusions in some of the furnace experiments.

Alloying Element	Sample	Observed Concentration (mean) wt.%	Standard Deviation	Matrix Concentration in wt.%	Analysed region & (method)
Manganese	F5	1.15	0.09	1.11	Allotriomorphic -
Chromium	F5	1.71	0.07	1.59	Acicular ferrite
Silicon	F5	0.44	0.51	0.51	colony (SEM)
Manganese	F6	1.24	0.13	1.11	Allotriomorphic -
Chromium	F6	1.74	0.14	1.59	Acicular ferrite
Silicon	F6	0.54	0.08	0.51	colony (TEM)
Manganese	F5	65.1	8.8	1.11	Inclusions
Chromium	F5	0.98	0.71	1.59	(Carbon replica)
Silicon	F5	26.76	9.1	0.51	(TEM)
Titanium	F5	5.4	5.0	0.009	

4.3.2 Dilatometry

The variety of microstructures obtained with changing austenite grain size are shown in Figs. 4.8 and 4.9. As expected, those specimens austenitised at the higher temperature of 1150 °C for 10 minutes transformed into allotriomorphic ferrite and acicular ferrite, whereas the others, austenitised at 1000 °C for 10 minutes transformed predominantly into a classical bainitic microstructure with a very small amount of allotriomorphic ferrite. The important observation again is that the presence of substantial amounts of acicular ferrite was associated with that of austenite grain boundary allotriomorphic ferrite.

The isothermal transformation experiments described in Table 4.4 were analysed further by plotting the relative length changes recorded during transformation as a function of the transformation temperature. To allow for any reaction before to reaching T_i, data at T_i were converted by linearly extrapolating the $\frac{\Delta L}{L}$- temperature curve for the temperature range T_γ to T_i. This is shown schematically in Fig. 4.10; the actual curves are shown in Fig. 4.11. The length changes recorded at T_i and those estimated by extrapolation to T_i were analysed further to deduce the degree of reaction at T_i (Table 4.6). The calculations also enable the carbon

concentration in the residual austenite to be estimated, *i.e.*, the experimental x_γ, which are marked on the calculated phase diagram shown in Fig. 4.12. The relative length change data obtained for all the dilatometric experiments indicate that some transformation could not be avoided before reaching T_i. As pointed out earlier, this is not important providing the total volume fraction of allotriomorphic ferrite is not very large.

Table 4.6 Volume fraction calculations:

Experiment	$(\frac{\Delta L}{L})_{max}$	Volume fraction transformed V	x_γ (Experimental) mole fraction	T_i °C
S1	0.0045	0.58	0.0053	505
S2	0.0042	0.54	0.0049	519
L1	0.0039	0.50	0.0045	513
L2	0.0035	0.45	0.0041	529

4.4 Discussion

It appears that, for the austenite grain size range studied here, the alloy used transforms into bainite (samples F3 and S1, S2) provided that the austenite grain boundaries are free to nucleate bainite. However, the transition from bainite to acicular ferrite can be stimulated by eliminating the austenite grain boundary nucleation sites (samples F4, F5 and L1, L2). The γ/γ boundaries were destroyed in effect by the formation of thin layers of grain boundary allotriomorphic ferrite in both adjacent γ grains. The transformation mechanisms for both acicular ferrite and bainite are also found to be similar, as confirmed by dilatometric experiments which gave results similar to those of Yang and Bhadeshia (1987a). The reaction clearly stopped at the point where $x_\gamma = x_{T_0'}$.

The important new observation is connected with the effect of the prior phase transformation to allotriomorphic ferrite. For the present alloy, the overall hardenability is low compared with the alloys studied by Yang and Bhadeshia. Since, allotriomorphic ferrite was not observed in their experiments, the observed transition from bainite to acicular ferrite with increasing grain size could be attributed simply to the decrease in grain boundary sites for the nucleation of bainite; as it is well established, classical bainite nucleation starts at the γ/γ grain boundaries (Bhadeshia, 1987a).

Thus, the present work gives an explanation of why high Cr welds tend to contain mostly bainite. Since the increase in Cr concentration reduces and eventually eliminates allotriomorphic ferrite, the austenite grain boundaries are free to nucleate the bainite before acicular ferrite can form intragranularly on the inclusions (Fig. 4.13).

Since both the acicular ferrite and bainitic ferrite reactions were found to terminate when x_γ reached $x_{T_0'}$, the results confirm that the transformation mechanisms for bainitic ferrite and acicular ferrite are similar. Thin film carbon replica analysis failed to show any carbide precipitation in all the samples supporting the assumption inherent in equation (2.1). The experimentally measured carbon concentration in the residual austenite at the point where the growth of acicular ferrite stopped, were found to be at somewhat lower carbon concentrations than estimated from the computed T_0' phase boundary (Fig. 4.12). This may be a consequence of a higher value of stored energy than that of 400 J mole^{-1} used in the present calculations.

The present results emphasise the fact the reactions taking place in the γ/γ grain boundaries can be crucial in determining the microstructures that develop in the weld metal. The ratio of the grain boundary and intragranular nucleation site densities can be modified to obtain the desired microstructure on transformation from austenite. The ability of inclusions to induce intragranular acicular ferrite is now a well established concept, though the nature and mechanism are not clear (Abson *et al.*, 1978, Dowling *et al.*, 1986, Ricks *et al.*, 1981, 1982, Liu and Olson, 1986 and Bhadeshia, 1989). Removal of inclusions clearly causes an acicular ferrite microstructure to change to one which contains bainite (Harrison and Farrar, 1981). This is also apparent in the measured continuous cooling transformation diagrams published by Homma *et al.*, (1987) which indicate that in the absence of oxide inclusions, austenite transforms into bainitic ferrite or Widmanstätten ferrite (Fig. 4.14). These two mechanisms are shown schematically in Fig. 4.13.

A search of the literature revealed that Cr and Mo are not the only elements to induce the formation of bainite at the expense of acicular ferrite. Similar effects can be deduced for manganese at high concentrations from the work by Horri *et al.*, (1988) and Grong *et al.*, (1986). In the latter work the "ferrite with aligned second phase" *i.e.*, (Widmanstätten ferrite or bainite) content was found to decrease with increase in Mn, as the acicular ferrite content increased. However, after an optimum level of manganese, the acicular ferrite began to be replaced to increasing degrees by "ferrite with aligned second phase", as the volume fraction of grain boundary allotriomorphic ferrite also decreased.

It remains to be explained why the layers of allotriomorphic ferrite themselves appear incapable of nucleating bainite. The reason could be associated with the fact that the α/γ interface may not be stationary at the temperature T_2. However, this is an unlikely explanation since

the reconstructive transformation of austenite to allotriomorphic ferrite is extremely sluggish at the temperatures where bainite forms. The alternative explanation is that the solute field, owing to elements displaced by the α into the adjacent γ, prevents the nucleation of bainite. If we consider the growth of allotriomorphic ferrite to occur by a paraequilibrium mechanism, then only the carbon composition profile ahead of the interface needs to be considered. With this assumption, consistent with the microanalysis data, allotriomorphic ferrite growth can be considered to be controlled by diffusion of carbon in the austenite ahead of the interface. The carbon composition profile in front of the moving interface can be calculated for various temperatures using the following equation (Coates, 1973b).

$$x\{X,t\} = \bar{x} + [x^{\gamma\alpha} - \bar{x}]\, E_1\{X, \underline{D}\} \tag{4.3}$$

where

$$E_1\{X, \underline{D}\} = \left[\frac{1 - erf\{X/(4\underline{D}t)^{0.5}\}}{1 - erf\{Z/(4\underline{D}t)^{0.5}\}}\right] \tag{4.4}$$

where X is the distance ahead of the the moving α/γ interface, Z is the thickness of the allotriomorphic ferrite grown after a time t from the initiation of growth, and $\underline{D}$ is the weighted average diffusivity of carbon in austenite given by Trivedi and Pound (1967).

The thickness of the allotriomorphic ferrite can be predicted using the equation (4.2). Since the growth took place while cooling, the value of Z and also of other variables should correspond to a condition where the allotriomorphic ferrite growth ceases. To simplify the problem the theoretical analysis was carried out for two cases: (i) the static case in which on cooling from T_1 to T_2, the carbon composition profile in the austenite does not change at T_2 and (ii) the dynamic case when the carbon tries to diffuse from a carbon enriched sessile α/γ interface to a more homogeneous composition throughout the residual austenite.

4.4.1 Static case

It is possible that the region of carbon enriched austenite in the vicinity of the allotriomorphic ferrite/austenite interface suppresses the nucleation of bainite at that interface. As the allotriomorphic ferrite formation temperature decreases, $x^{\gamma\alpha}$ increases and the W_S, B_S and M_S temperatures of austenite of composition $x^{\gamma\alpha}$ decrease, as illustrated in Fig. 4.15b. The transformation temperatures were all calculated according to Bhadeshia (1981a, 1982a). If the isothermal transformation temperature T_2 is above the calculated W_S or B_S temperatures for the austenite at the α/γ interface, then it can be concluded that the interface is incapable of nucleating Widmanstätten ferrite or bainite. Such a situation arises for all temperatures below the point marked 'A' ($\simeq$ 720 °C) on Fig. 4.15b. Since T_2 was in the present case always below 720 °C, the calculations are consistent with the result that no Widmanstätten ferrite or bainite

could be observed to nucleate from α/γ interfaces, thus making the allotriomorphic ferrite ideal for the purpose of stimulating the intragranular growth of α_a.

4.4.2 Dynamic case

This above model may not be valid if the carbon concentration profile at the α/γ interface homogenises during heat treatment at T_2. The growth of allotriomorphic ferrite becomes very sluggish indeed at temperatures below B_S and it is assumed here that it actually stops, thereby providing opportunity for homogenisation. A finite difference method (see Appendix) was used to test whether the carbon concentration profile, which develops during the growth of allotriomorphic ferrite at T_1, changes sufficiently on holding at T_2, to enable the austenite in the vicinity of the α/γ interface to decompose to bainite. The initial composition profile was established using equation (4.3) and assuming the allotriomorphic ferrite thickness is about 5 μm .

The calculations are carried out for $T_1 = T_C$, where T_C is the temperature where the upper and lower 'C' curves of the TTT diagram intersect. At T_C, displacive reactions become kinetically favoured after reconstructive transformations, so that T_C can be assumed to be the temperature at which the allotriomorphic ferrite growth stops. The homogenisation of carbon on subsequent treatment at $T_2 = 470$ °C is illustrated in Figs. 4.16 and 4.17. Even after holding for 120 seconds at T_2 (the longest reaction time used in the experiments), the calculations proved that the carbon content in the enriched austenite at the α/γ interface remains high enough to prevent the formation of bainite.

It is of interest to examine other possible methods for rendering the austenite grain surfaces ineffective as possible bainite nucleation sites. The work of Mori *et al.*, (1980) Snieder and Kerr (1984) and Fleck *et al.*, (1986) in which boron is used as an alloy addition is relevant this respect. Finally, it should be noted that it may may not be necessary to completely cover the austenite grain boundaries with allotriomorphic ferrite, since the ferrite will nucleate first at the most potent sites, thus eliminating them for the purpose of bainite nucleation. It is also relevant to point out that fewer than half of the allotriomorphic ferrite layers are likely to be in a crystallographic orientation suitable to stimulate α_W or α_b growth even if the enriched austenite of γ at the α/γ interface did not prevent such growth. The reported increase in the acicular ferrite by Snieder and Kerr (1984) using boron additions implies that the procedure could be considered for stimulating acicular ferrite in Fe-Cr-Mo-C welds also.

4.5 Conclusions

It is found that in weld metals containing inclusions the transition from bainite to acicular ferrite can be stimulated by the prior formation of a small amount of allotriomorphic ferrite

along the austenite grain surfaces. This could be one of the main reasons why Fe-Cr-Mo-C welds tend to have predominantly bainitic microstructures at high alloy concentrations, since the allotriomorphic ferrite formation is then suppressed. Providing that the austenite grain boundaries are free to nucleate bainitic ferrite, the latter phase, in general cannot be avoided and its formation will lead to a corresponding reduction in the quantity of acicular ferrite. It is probable that any allotriomorphic ferrite which is in a suitable orientation relationship to stimulate bainite cannot in fact do so, because the solute concentration in the enriched austenite at the allotriomorphic ferrite/austenite interface prevents it from transforming to bainite. This hypothesis has been confirmed using finite difference analysis which indicated that the time taken for the carbon to homogenise is much higher than that required for α_a formation.

APPENDIX

Finite difference method

The carbon composition profile build up ahead of the allotriomorphic ferrite / austenite interface in the residual austenite, is examined here using a finite difference method to simulate any homogenisation of concentration. The main advantage of the application of finite difference method to this problem is that it can handle the changing boundary conditions during the homogenisation process. The finite difference method is based on the technique discussed by Crank (1975). The model assumes a one dimensional diffusion process ahead of a planar allotriomorphic - austenite interface. The initial profile set up at a time $t = 0$, is given by the analytical equation as discussed in the main text. The composition profile is then subjected to finite difference method after normalising the variables to dimensionless quantities suitable for this method. The normalised variables are as follows

$$Distance\ X = \frac{x}{(\frac{\gamma_{g.s}}{2} - q)}$$

$$Concentration\ C = \frac{C_{i,j}}{C^{\gamma\alpha}}$$

$$Time\ T = \frac{\underline{D}t}{x^2}$$

where x is the distance from the α/γ interface, q is the half thickness of ferrite and $\gamma_{g.s}$ is the austenite grain size. $C_{i,j}$ is the composition at any time step j and at position i from the interface and $C^{\gamma\alpha}$ is the composition of interface at $t = 0$. $\underline{D}$ is the average diffusivity calculated for every time step δt. Here the interface position does not move with time, since allotriomorphic ferrite growth is assumed to be completed. The interface composition is determined for each time step by the mass balance. The area under the normalised composition profile is calculated using numerical integration. The general finite difference equation for the composition in the next time interval is

$$C^{\gamma}_{i,j+1} = C^{\gamma}_{i,j} + R(C^{\gamma}_{i-1,j} - 2C^{\gamma}_{i,j} + C^{\gamma}_{i+1,j})$$

where $R = \underline{D}\delta t/(\delta x)^2$, and is taken to be 0.1. This particular value was assumed after checking that variation of R coefficient from 0.1 - 0.3 made negligible difference to the results. $C^{\gamma}_{i,j+1}$ is the composition at i position of interface and at a time step $j + 1$ and is derived from the compositions at the $i-1, i, i+1$ positions at a time step of j. The diffusivity for next time step is calculated from the composition profile for the current time. The flow chart for the program is presented in Fig. 4.18.

a

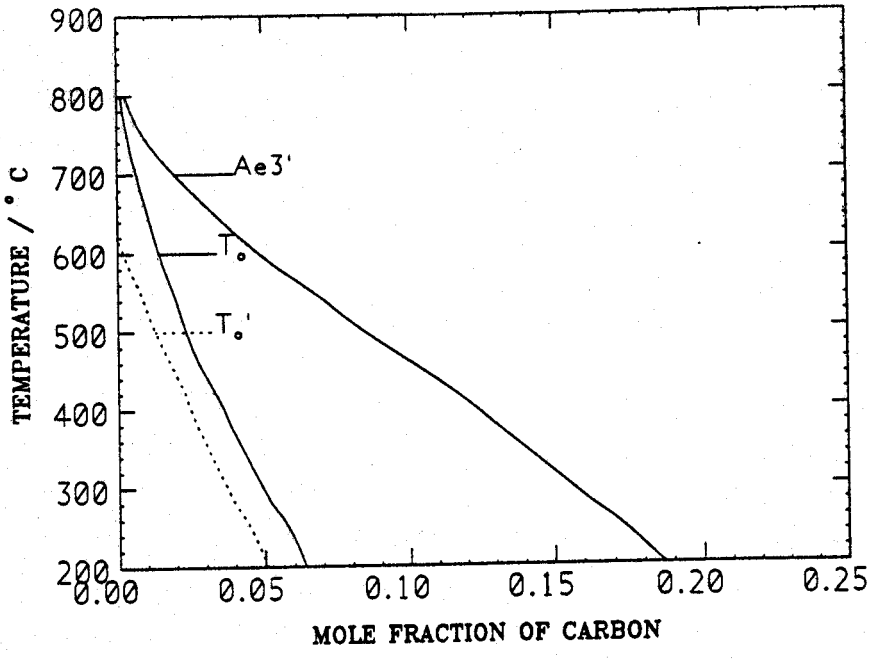

b

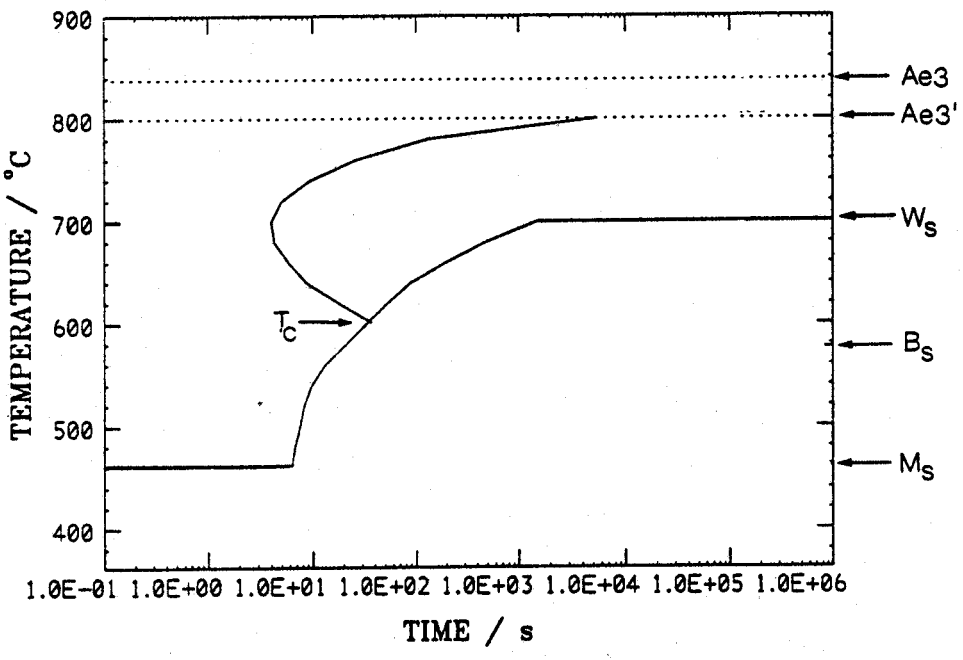

Fig. 4.1 Calculated (a) phase diagram and (b) TTT diagram based on the model developed by Bhadeshia (1981a, 1982a) for Fe - 0.053C - 0.51Si - 1.11Mn - 1.59Cr (wt.%) weld metal.

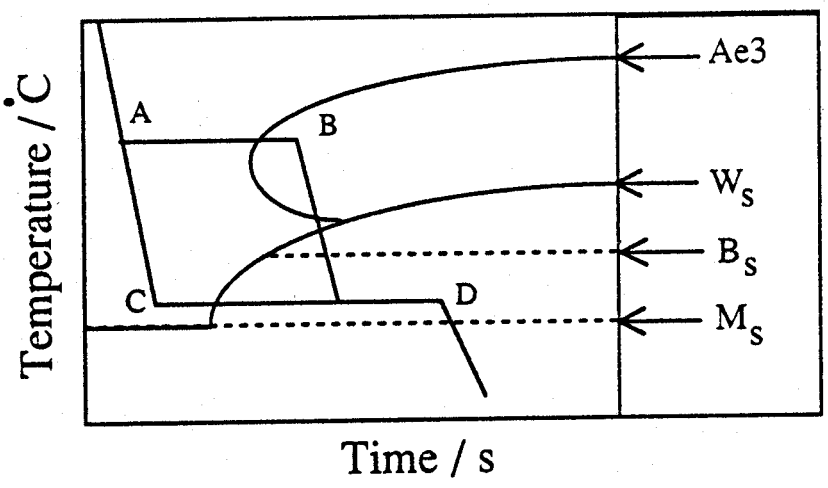

Fig. 4.2 Schematic illustration of the furnace heat treatments: The path ABD shows a two step heat treatment, and ACD a single step heat treatment, respectively; Three resistance heated furnaces were used.

a

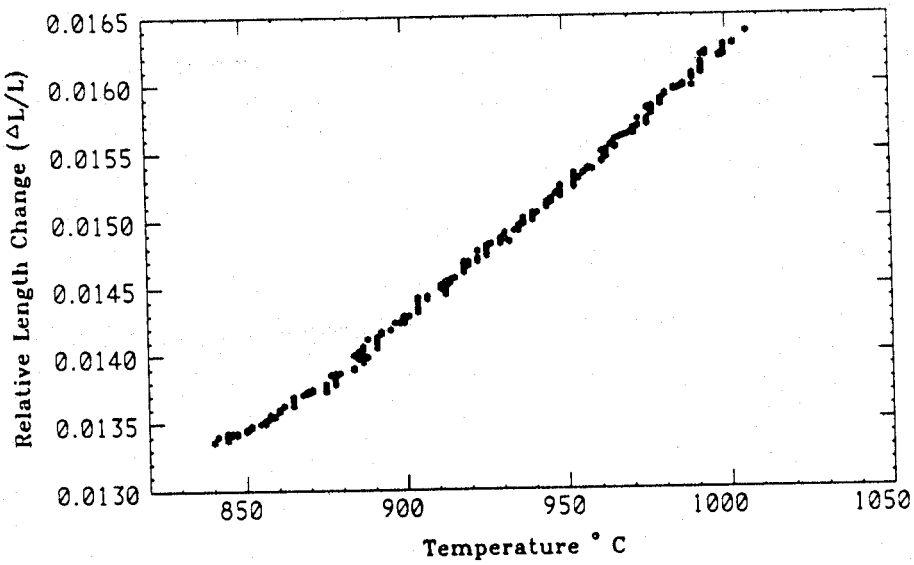

b

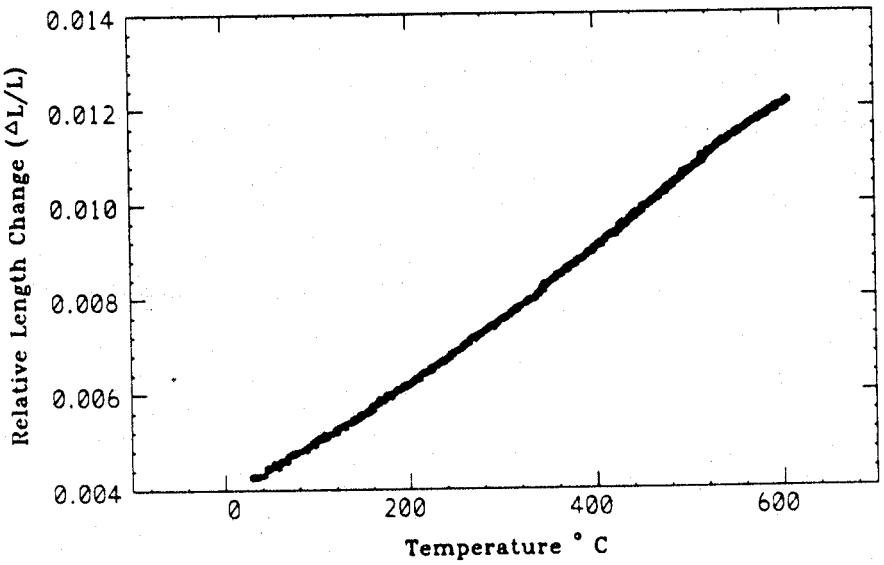

Fig. 4.3 Typical data used for measurement of (a) austenite and (b) ferrite linear thermal expansion coefficients. The correlation coefficient of the data were found to be more than 0.99, when subjected to linear regression analysis.

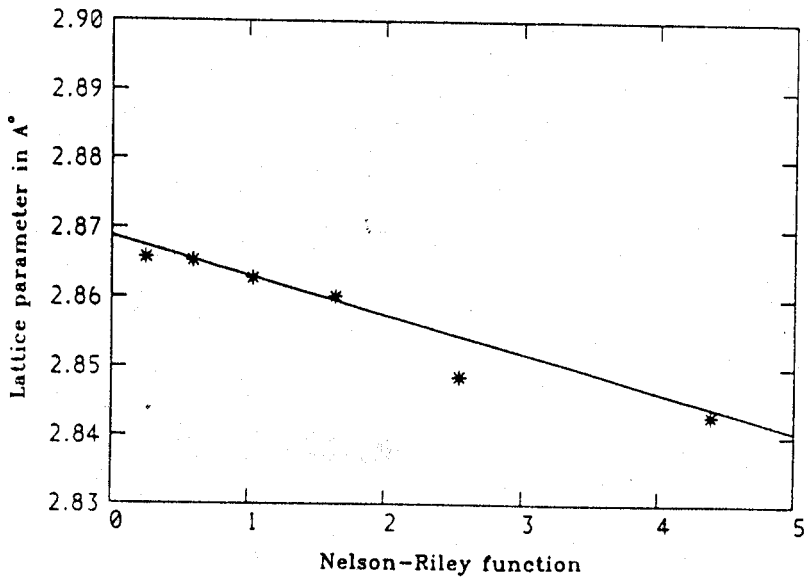

Fig. 4.4 Lattice parameter measurement by extrapolation of Nelson-Riley function (see section 2.4): points represent the lattice parameter measured from the angles measured from various sets of planes; solid line is the fitted line with weighting; and the intercept at Y axis for Nelson-Riley function value of zero gives the lattice parameter of ferrite.

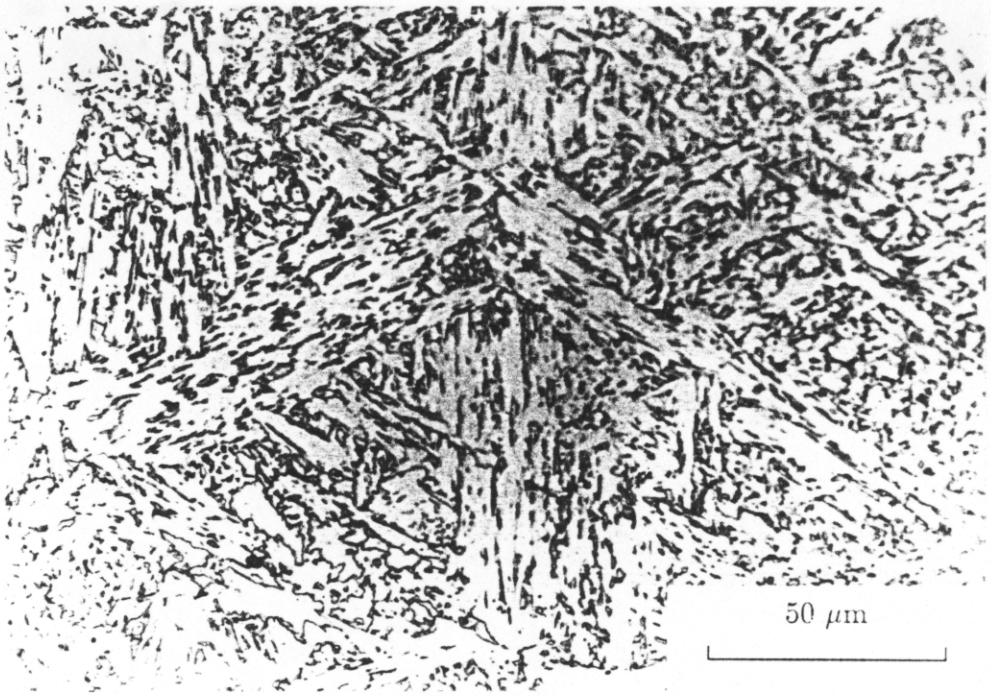

a

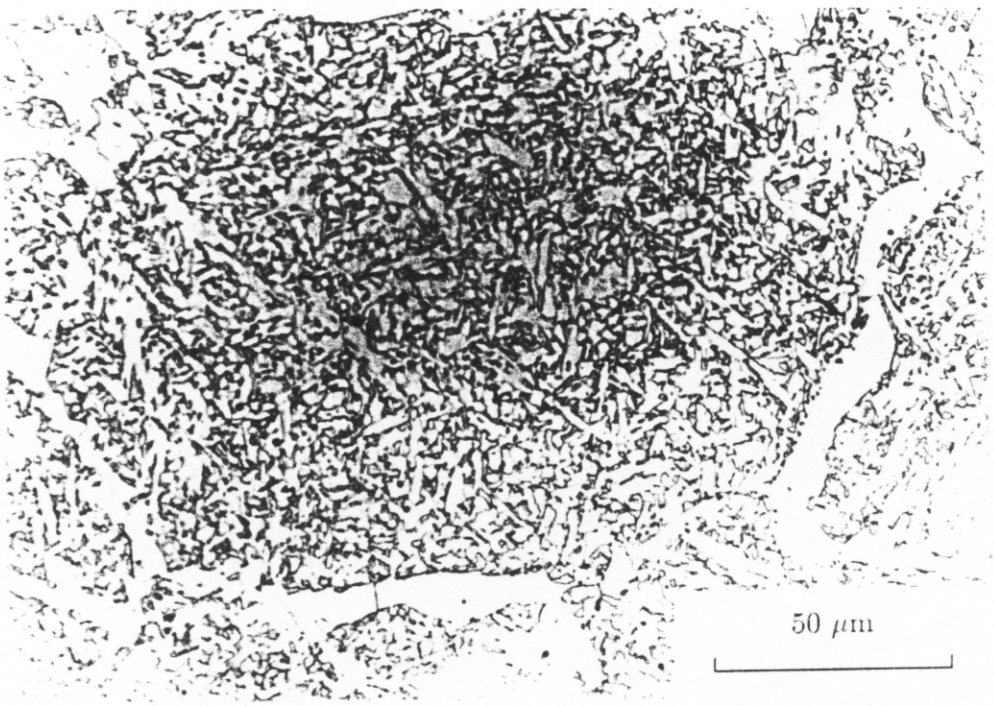

b

Fig. 4.5 Microstructures obtained in the furnace experiments F3-5.

a. F3; Microstructure depicting bainitic sheaf structure (microhardness measured was 278 HV).

b. F4; Microstructure of acicular ferrite and grain boundary allotriomorphic ferrite (microhardness of acicular ferrite region was 285 HV).

c

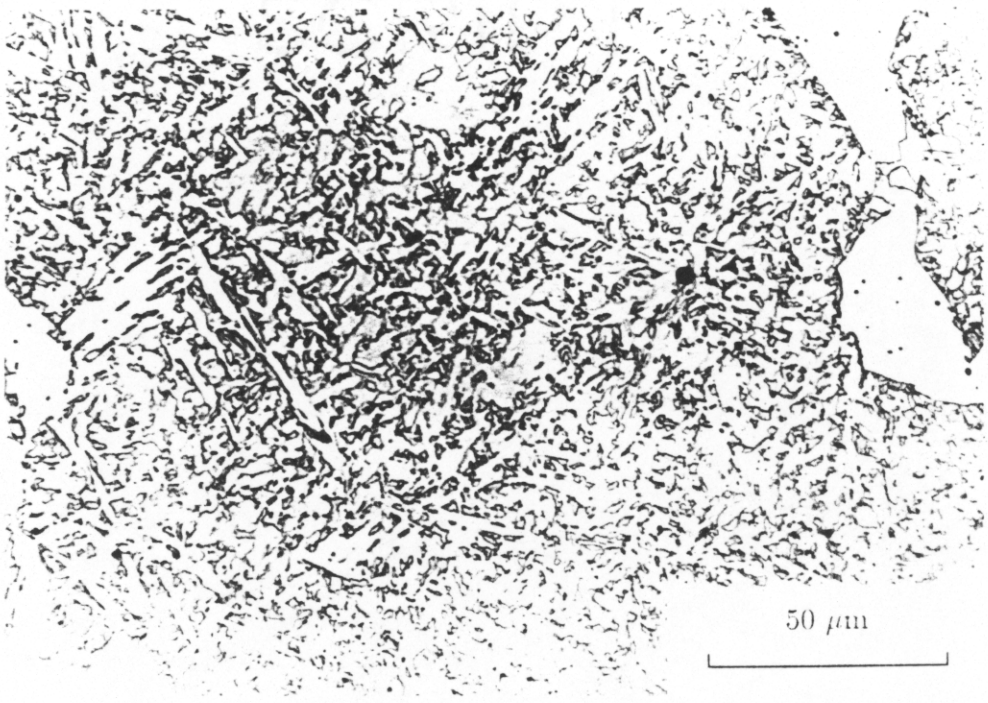

Fig. 4.5 continued....

c. F5; Microstructure of allotriomorphic ferrite and acicular ferrite; note that the thickness of allotriomorphic ferrite is bigger than F4 (microhardness measured in the acicular ferrite region was 283 HV).

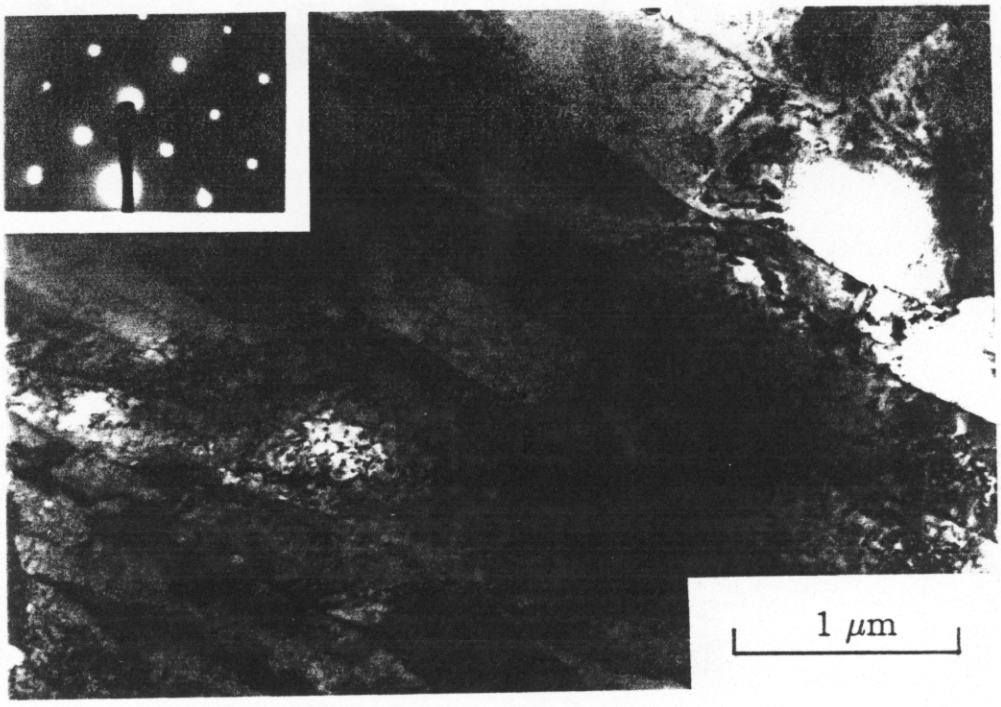

d

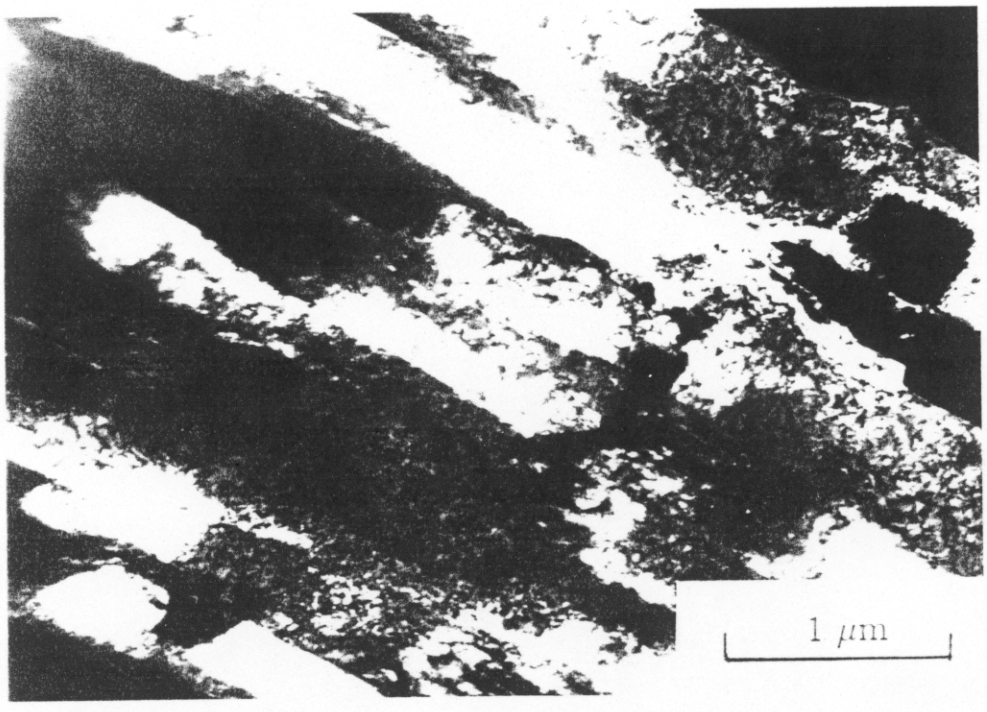

e

Fig. 4.5 continued....

d. F3; Bright field image illustrating the sheaf structure of bainite (inset is the diffraction pattern from a < 001 > ferrite zone axis)

e. F3; Corresponding dark field image using (020) spot, showing that the bainitic platelets within the sheaf are all in the same crystallographic orientation.

f

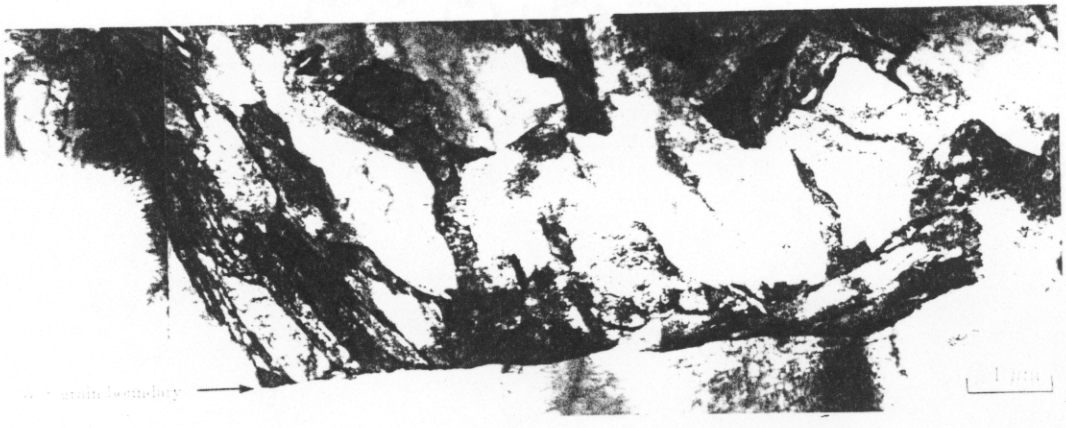

f. F5; microstructure indicating possible acicular ferrite nucleation away from the α/γ interface (dark phase could be martensite transformed from carbon enriched austenite).

a

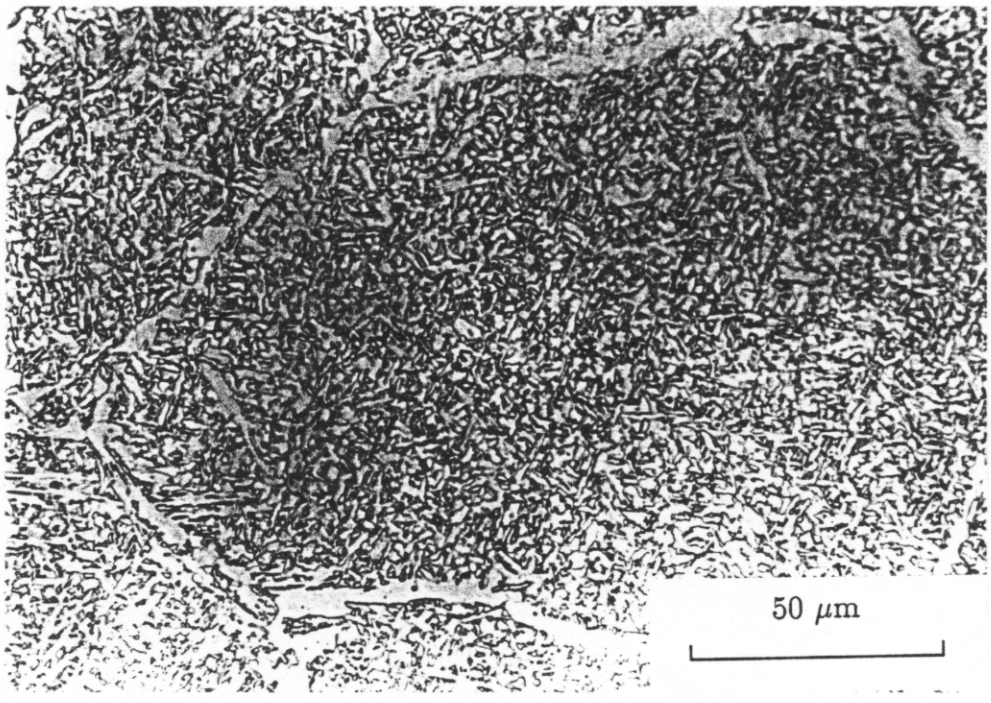

Fig. 4.6 Microstructures obtained in the furnace experiments F6-8.

a. F6; Microstructure on transformation by continuous cooling (note the similarity between this microstructure and the typical weld microstructures that develop in ordinary C-Mn weld metals).

b

Fig. 4.6 continued....

b. F6; Typical microstructure developed near to α/γ interface. The microstructure depicts the allotriomorphic ferrite and acicular ferrite colony away from the interface. The dark phase could be martensite formed from the carbon enriched austenite

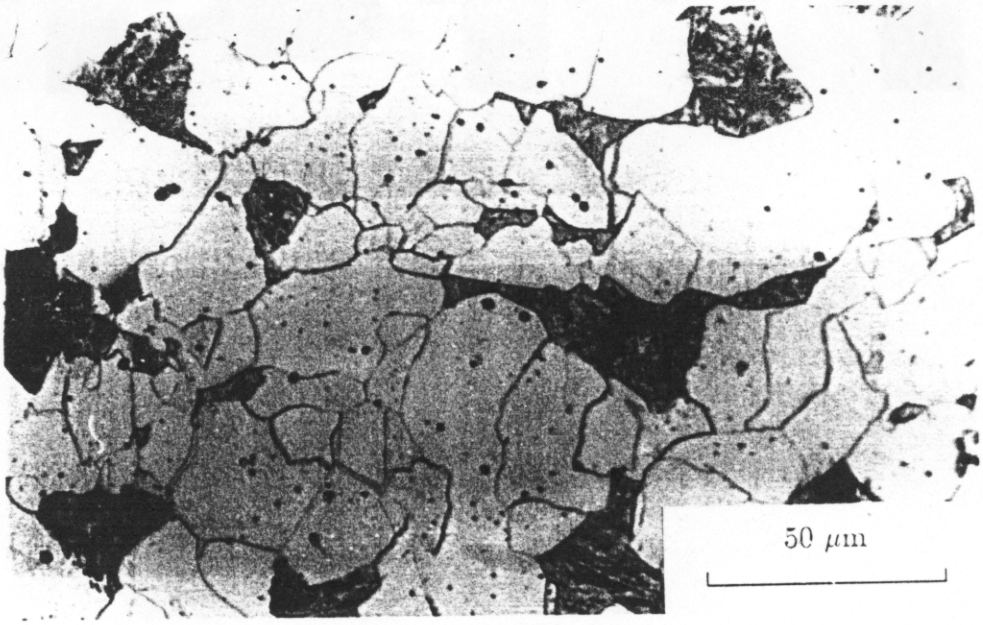

c

d

Fig. 4.6 continued....

c. F7; Microstructure developed by transformation above B_S, T_2=600 °C after T_1=800 °C; the microstructure is essentially allotriomorphic ferrite and martensite.

d. F8; The residual austenite islands transformed to martensite by quenching after T_1=800 °C; proving the fact that the acicular ferrite morphology develops only by transformation below B_S. The hardness measured in the martensitic region was found to be 352 HV and that of allotriomorphic ferrite was found to be 193 HV.

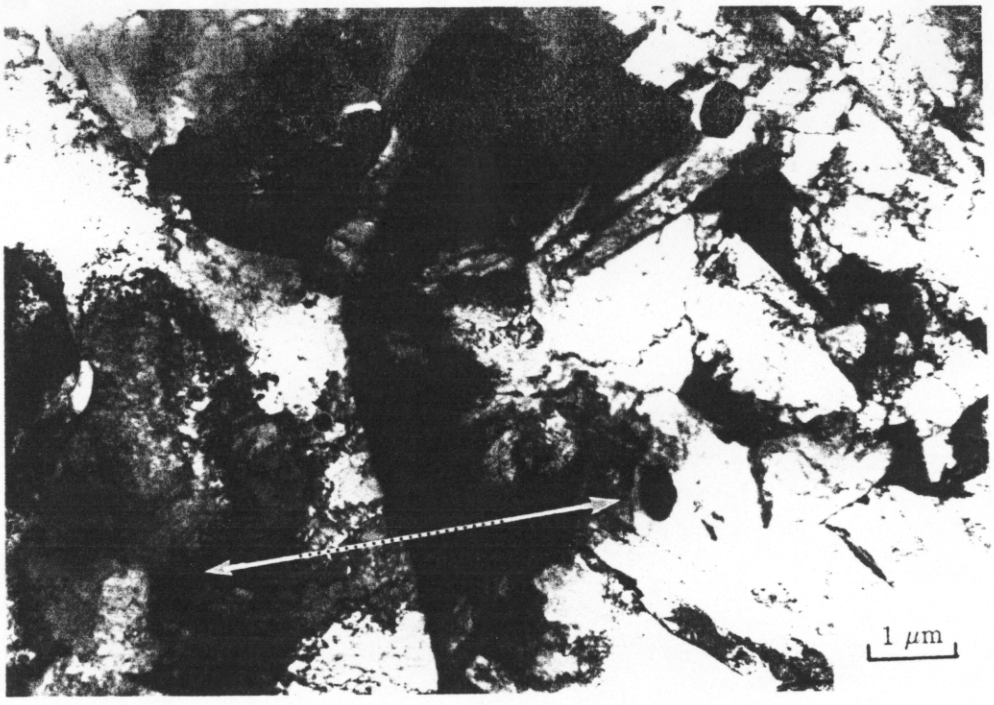

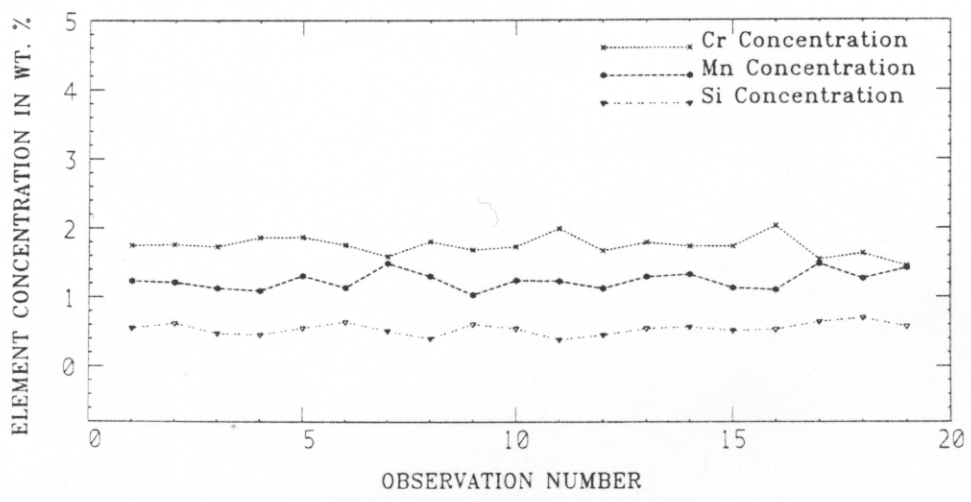

Fig. 4.7 Details of EDX analysis on samples from furnace experiments.

a. Region analysed by EDX in TEM, in the sample F6, across an allotriomorphic ferrite and an acicular ferrite colony. The line represents the region over which the analysis were carried out.

b. Variation of Si, Mn and Cr as measured by the EDX analysis over a line as shown in the Fig. 4.7a. The first 10 points correspond to the allotriomorphic ferrite region and the rest to acicular ferrite colony. The variation shows no systematic change in alloying element concentration.

c

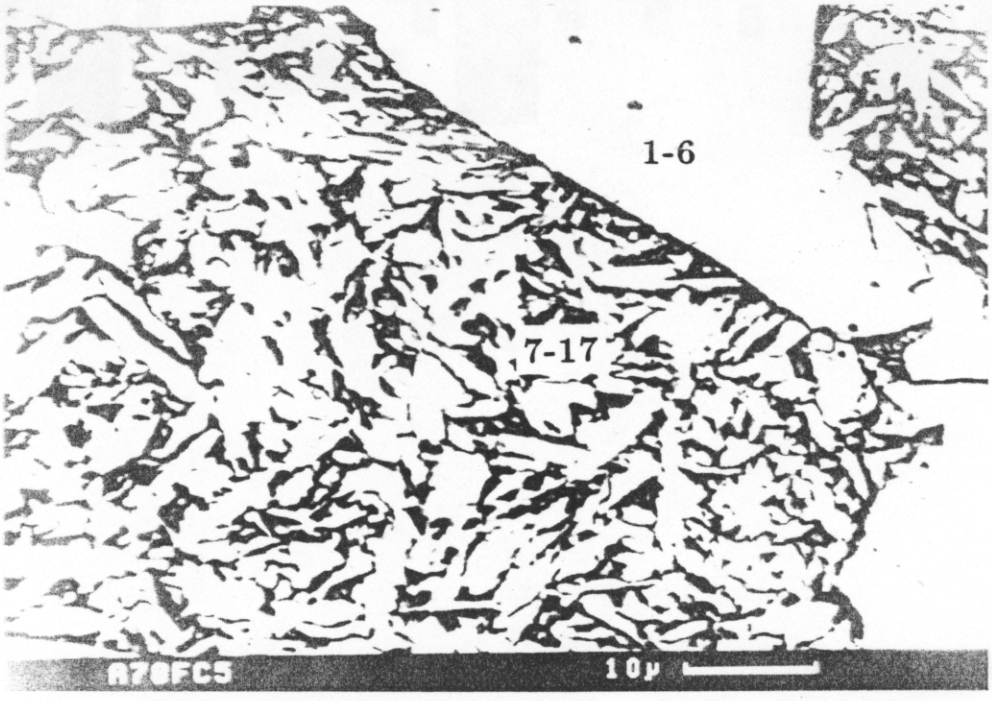

d

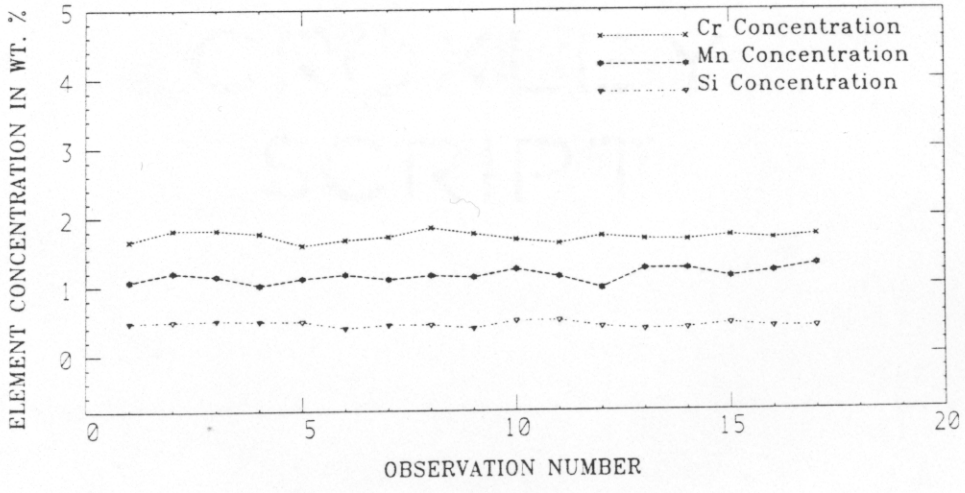

Fig. 4.7 continued....

c. The allotriomorphic ferrite and acicular ferrite microstructure as observed in SEM, which was subjected to EDX analysis.

d. Variation of Si, Mn and Cr as measured by EDX analysis over the spots as shown in the Fig. 4.7c. The points 1-6 correspond to the analysis obtained from allotriomorphic ferrite region and rest from the acicular ferrite region.

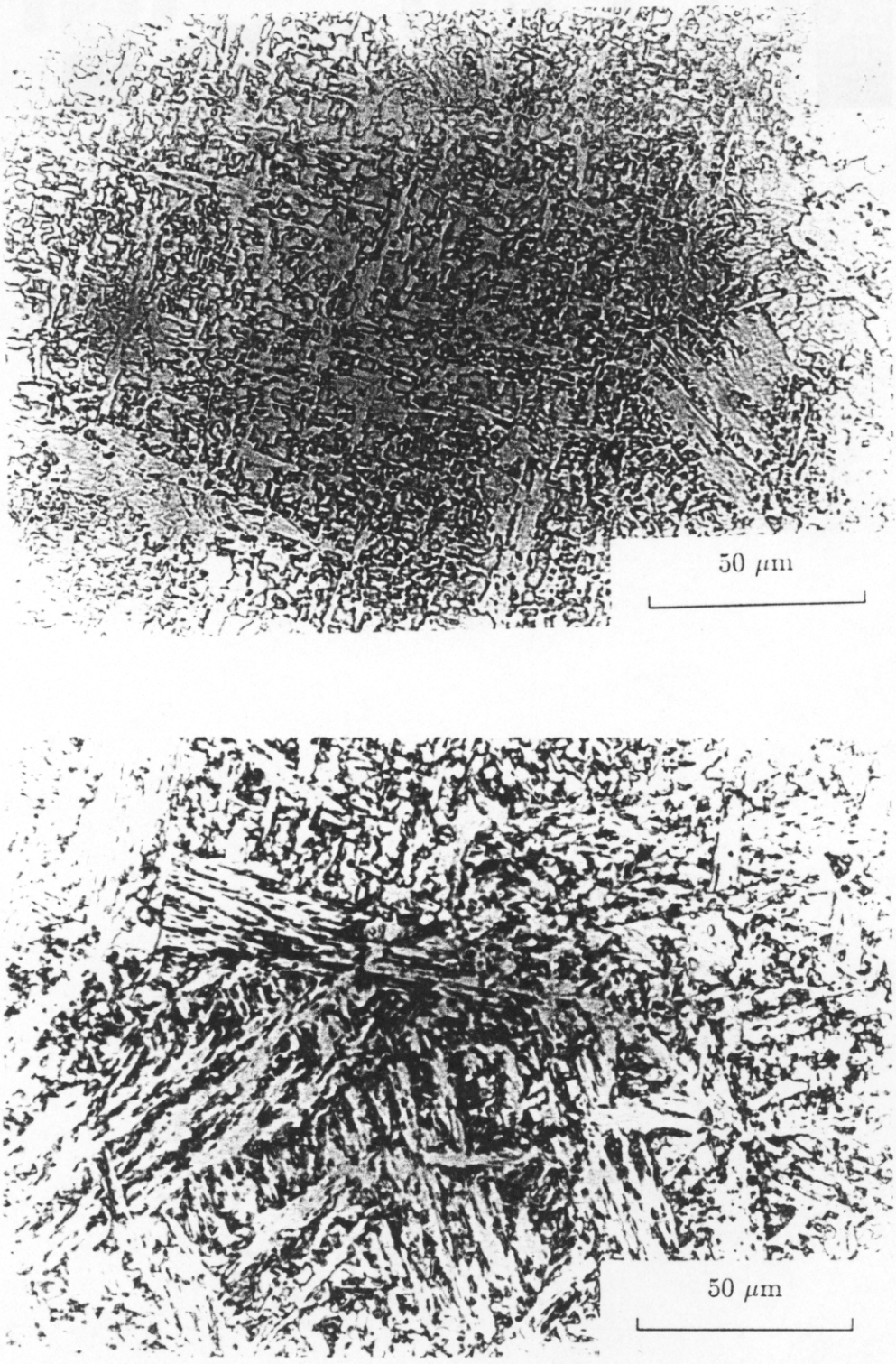

Fig. 4.8 The comparison microstructure of isothermally transformed samples from dilatometric experiments.

a. L1; Illustrating the effect of allotriomorphic ferrite on promoting acicular ferrite

b. S1; Microstructure of predominantly bainite: no grain boundary allotriomorphic ferrite can be seen.

a

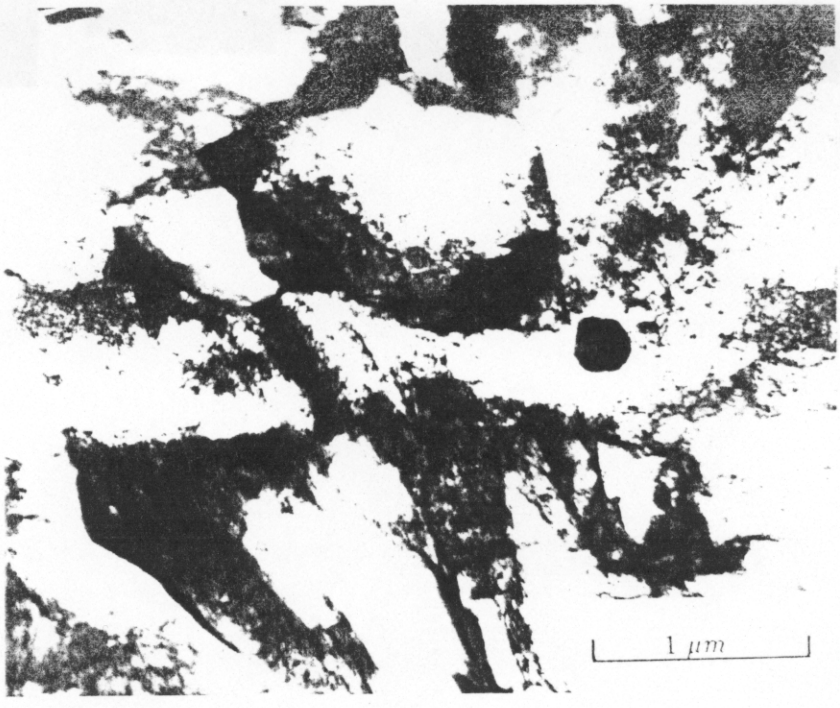

b

Fig. 4.9 Transmission electron micrographs of isothermally transformed samples in dilatometric experiments:

a. L1; Typical acicular ferrite plates nucleating from inclusion and also the impingement of that plate with nearby plates also could be observed.

b. S1; Bainitic sheaf structure nucleating from prior γ/γ interface. Inclusions are also seen along the grain boundary.

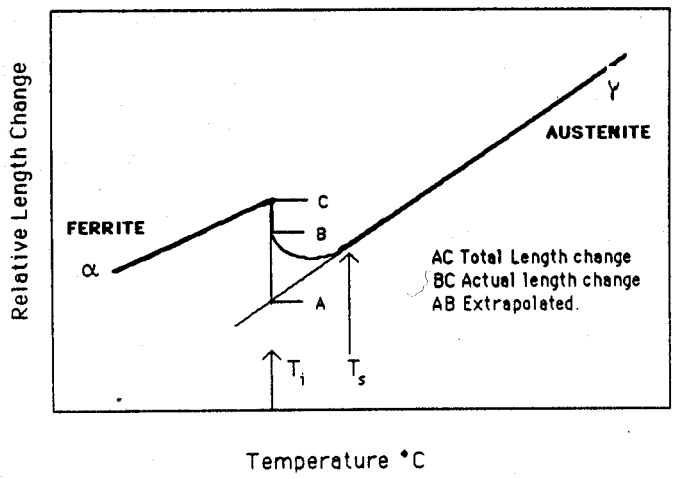

Fig. 4.10 Schematic diagram illustrating the extrapolation method to calculate the maximum relative length change at isothermal heat treatment temperature (T_i); given a case where there is transformation before reaching the temperature T_i while cooling from austenite phase field. The dark line indicates the actual relative length change.

a

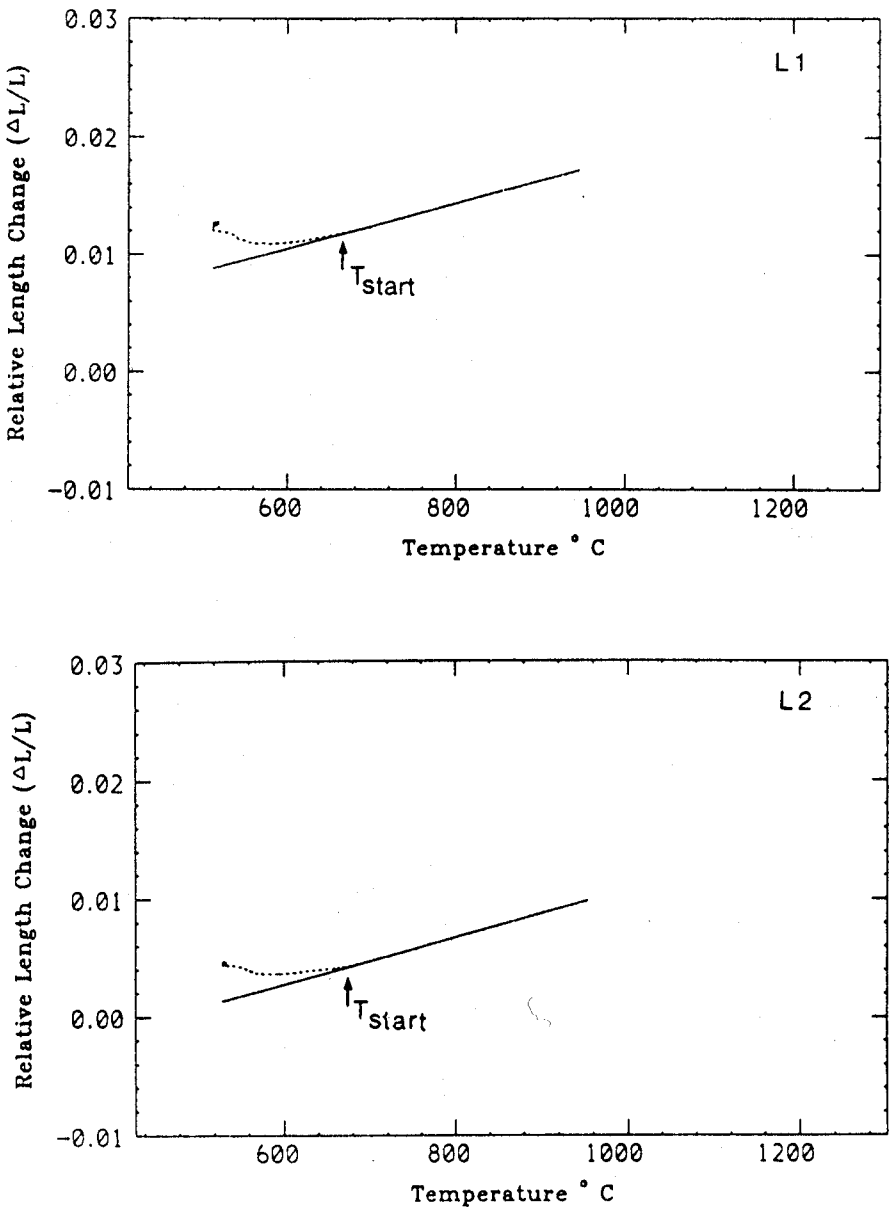

Fig. 4.11 Comparison of $\frac{\Delta L}{L}$- temperature plots for the dilatometric experiments as mentioned in Table 4.4. The plots show the transformation start temperature and extrapolation procedure for calculating the maximum length change at T_i.

a. L1 and L2; After T_S, the transformation rate seem to be very high as indicated by its rate of slope change of actual $\frac{\Delta L}{L}$-Temperature curve from extrapolated straight line. This indicates the allotriomorphic ferrite transformation while cooling from T_γ. This is also supported by high Δt_{850-T_i} (Table 4.3).

b

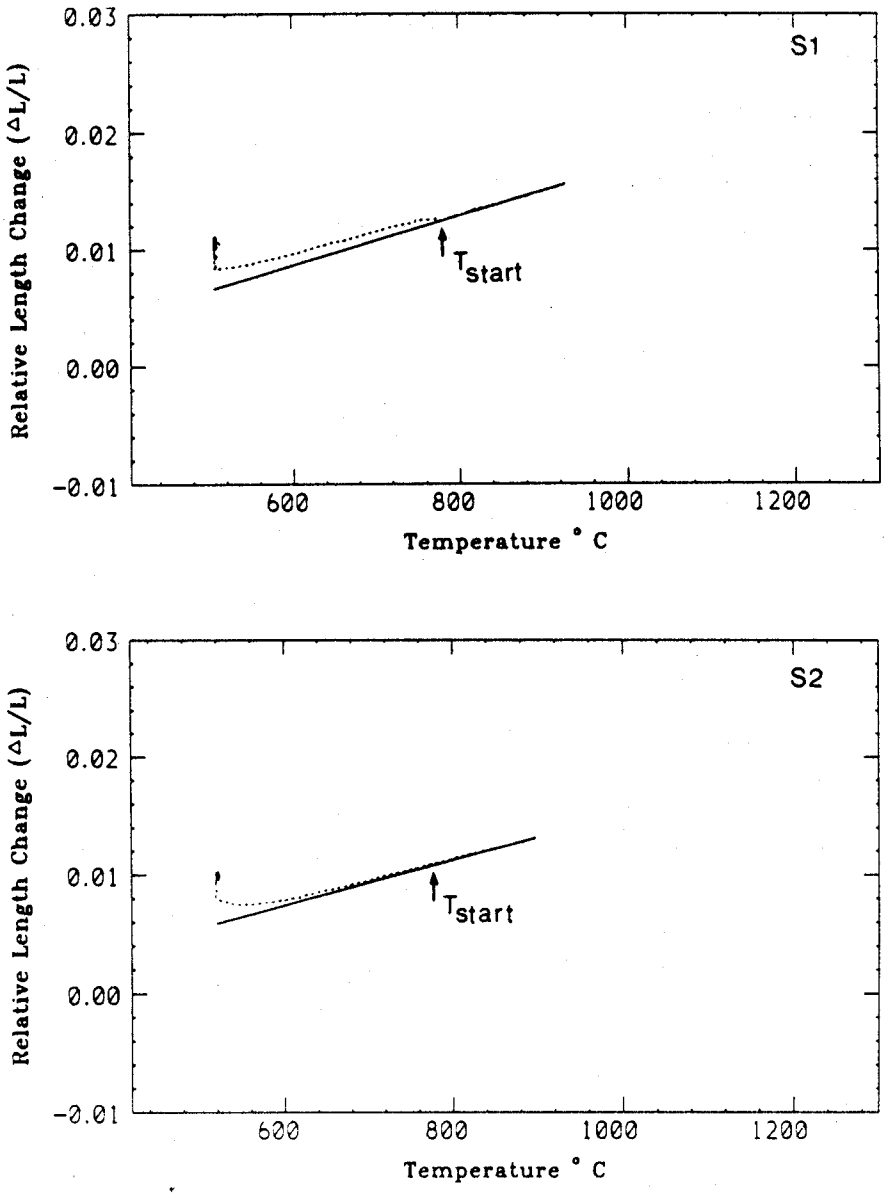

Fig. 4.11 continued....

b. S1 and S2; Though the transformation started at very high temperature, as seen in the graph, because of less Δt_{850-T_i} (Table 4.3), the transformation to allotriomorphic ferrite was comparatively less. This can be reasoned from the rate of slope change of the actual $\frac{\Delta L}{L}$-Temperature curve with respect to extrapolated straight line.

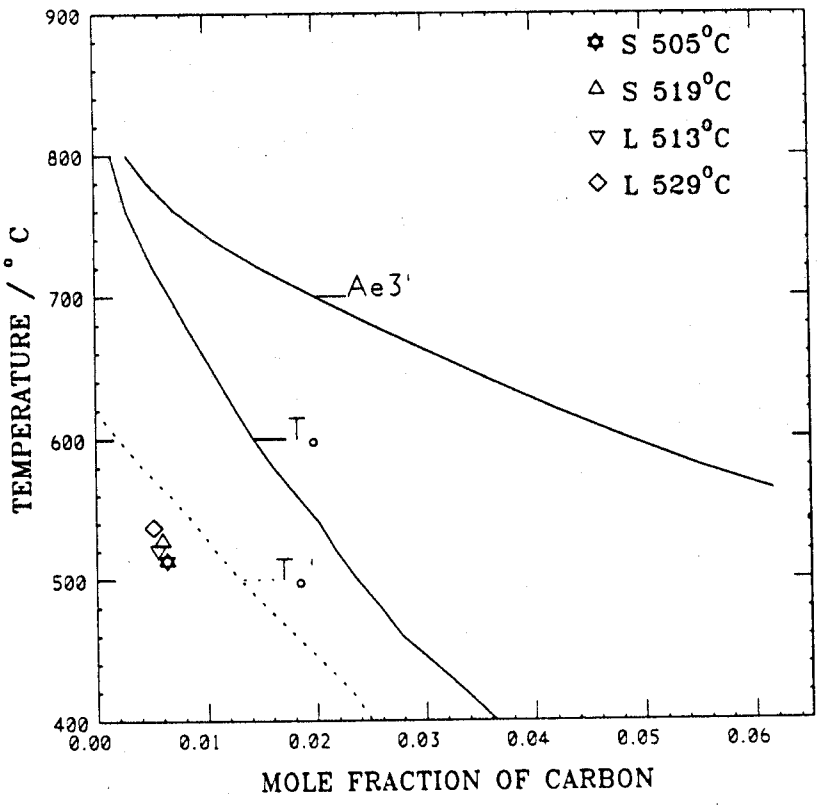

Fig. 4.12 Comparison of experimental x_γ points corresponding to maximum volume fraction of ferrite for the dilatometer experiments and the phase boundary line calculated by Bhadeshia (1981a, 1982a). L represents high T_γ specimens and S represents low T_γ specimens.

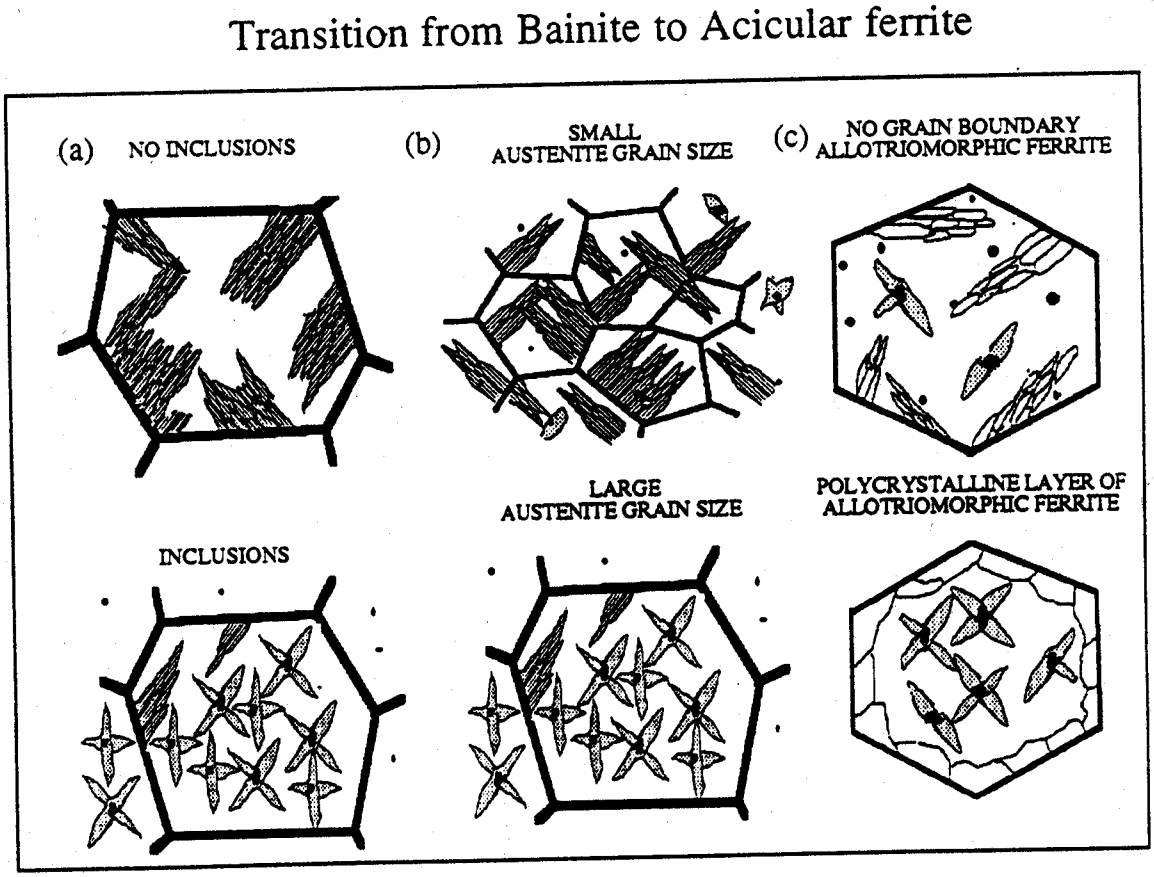

Fig. 4.13 Schematic illustration of mechanisms of transition from acicular ferrite to bainite due to the published ones and also due to the present results (see next page).

a. Effect of varying inclusion density for the same austenite grain size.

b. Effect of varying austenite grain boundary nucleation site density (grain size effect)

c. Effect of prior transformation to allotriomorphic ferrite for the same austenite grain size.

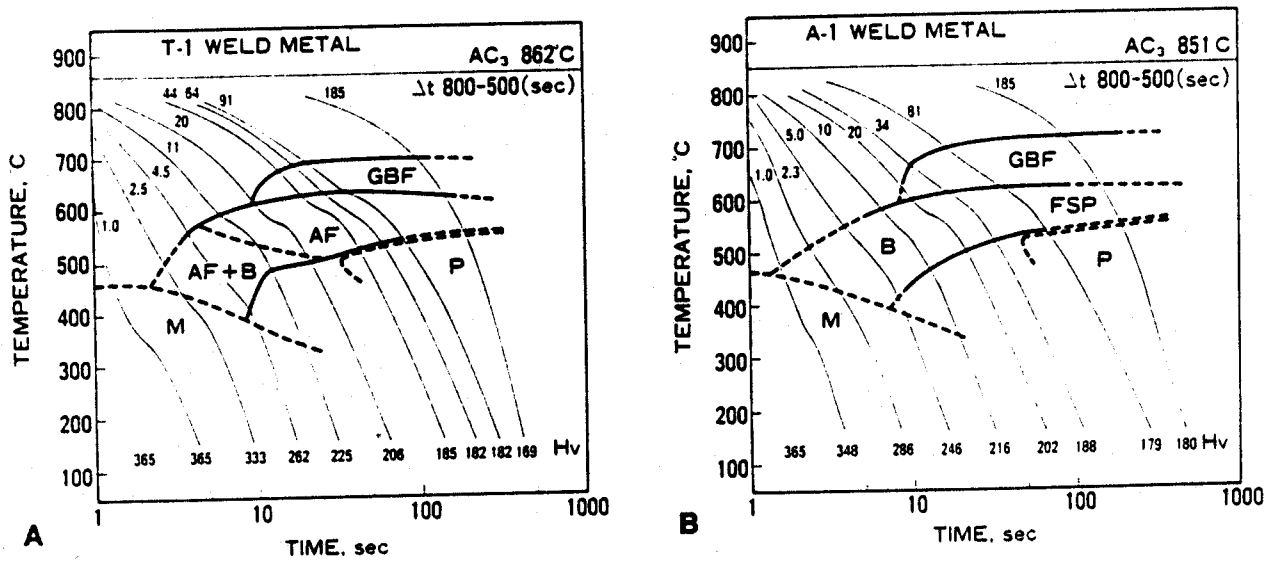

Fig 2 – CCT diagrams. A – Ti-oxide-containing weld metal (T-1); B – Ti-oxide-free weld metal (A-1)

Fig. 4.14 Comparison CCT diagram for the weld metal containing Ti_2O_3 and no Ti_2O_3, after Homma *et al.*, (1987). The region B represents bainite and AF represents acicular ferrite. The presence of Ti_2O_3 promotes the formation of acicular ferrite.

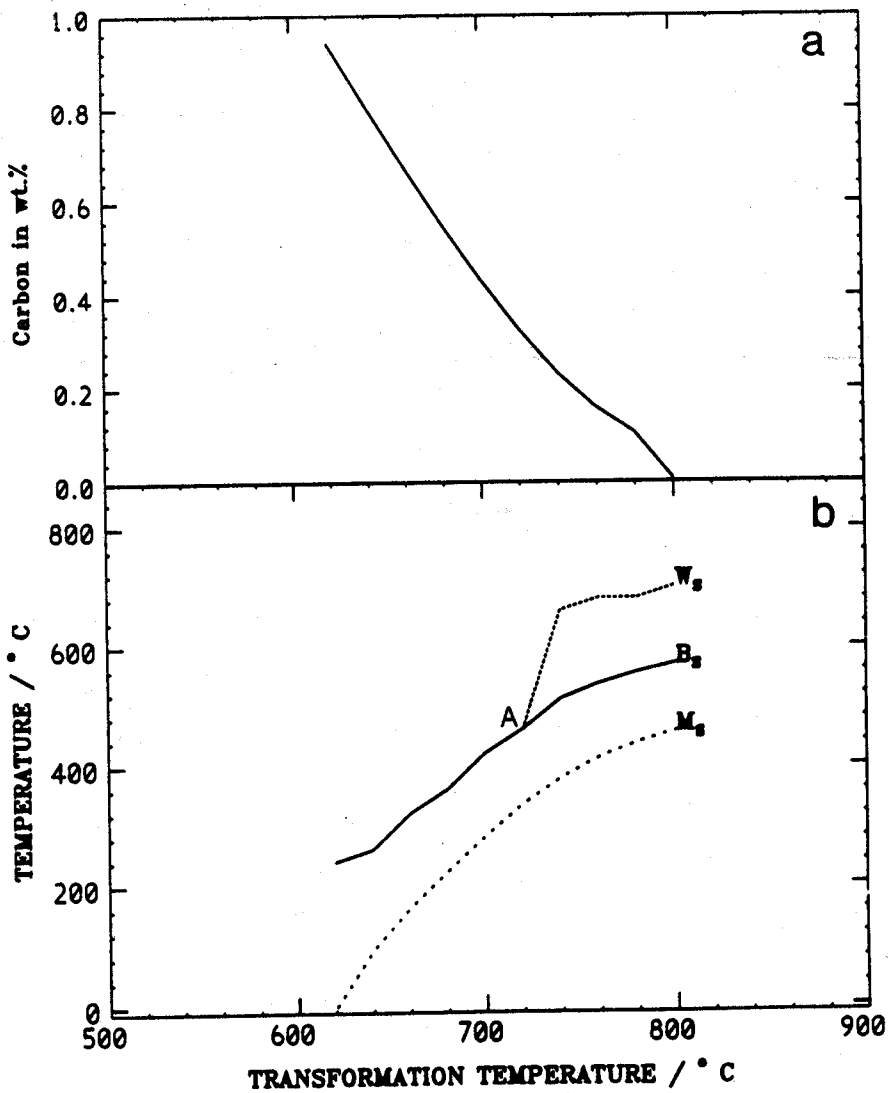

Fig. 4.15 The diagrams illustrate the condition for nucleation of bainite at the allotriomorphic ferrite/austenite interface. The upper graph is essentially a representation of the Ae_3' phase boundary line for the present alloy. If the second isothermal transformation temperature is higher than the calculated W_S or B_S temperatures then the nucleation of Widmanstätten ferrite or bainite is impossible. The point A represents the lowest allotriomorphic ferrite transformation temperature below which the α/γ interface is found not to be capable of nucleating Widmanstätten ferrite or bainite.

a. Variation in $x^{\gamma\alpha}$ as a function of the temperature at which allotriomorphic ferrite grows.

b. Variation in W_S, B_S and $M_S$temperatures of the austenite at the allotriomorphic ferrite / austenite interface, as a function of the transformation temperature at which the allotriomorphic ferrite grows by paraequilibrium transformation.

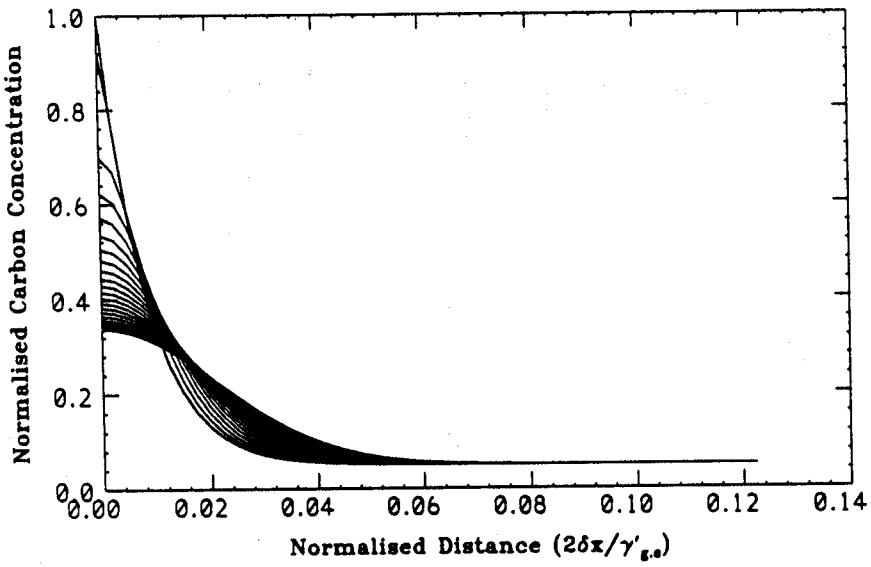

Fig. 4.16 The cascade of carbon composition profile for a time duration of 120 seconds at T_2=470 °C. The graph was drawn by normalising interface composition with respect to initial interface composition and the distance by half value of $\gamma'_{g.s}$ (residual austenite grain size). The initial profile set up was calculated as discussed in the text for a transformation temperature of 600 °C. The figure shows that in the time period at $T_2$the carbon composition neither gets homogenised nor reduces to certain level that point A could be reached as explained in static case. (This analysis assumes there is no change in the interface composition as it cools to T_2).

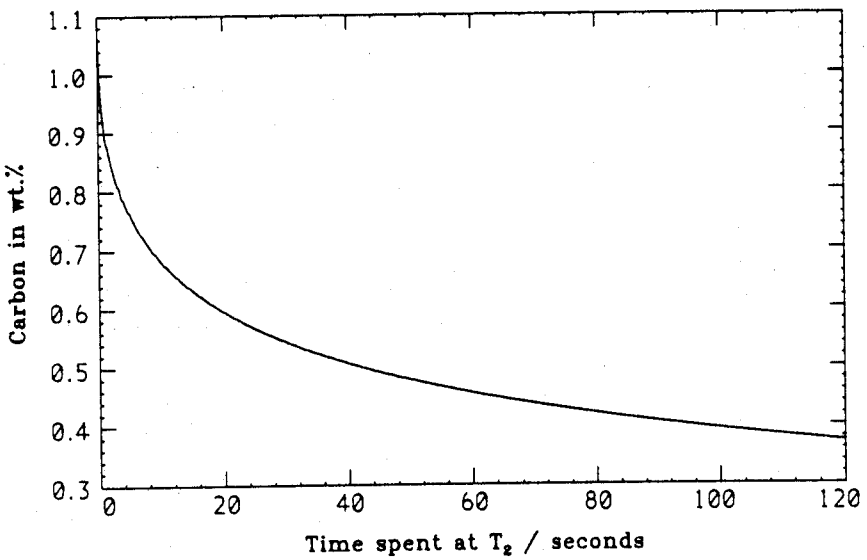

Fig. 4.17 The cascade of interface composition only with respect to time at T_2=470 °C. The interface composition only drops to 0.358 wt.% which is still less than the point A for the condition for nucleation of bainite at allotriomorphic - austenite interface. Before this could be achieved the intragranular inclusions could stimulate the formation of acicular ferrite.

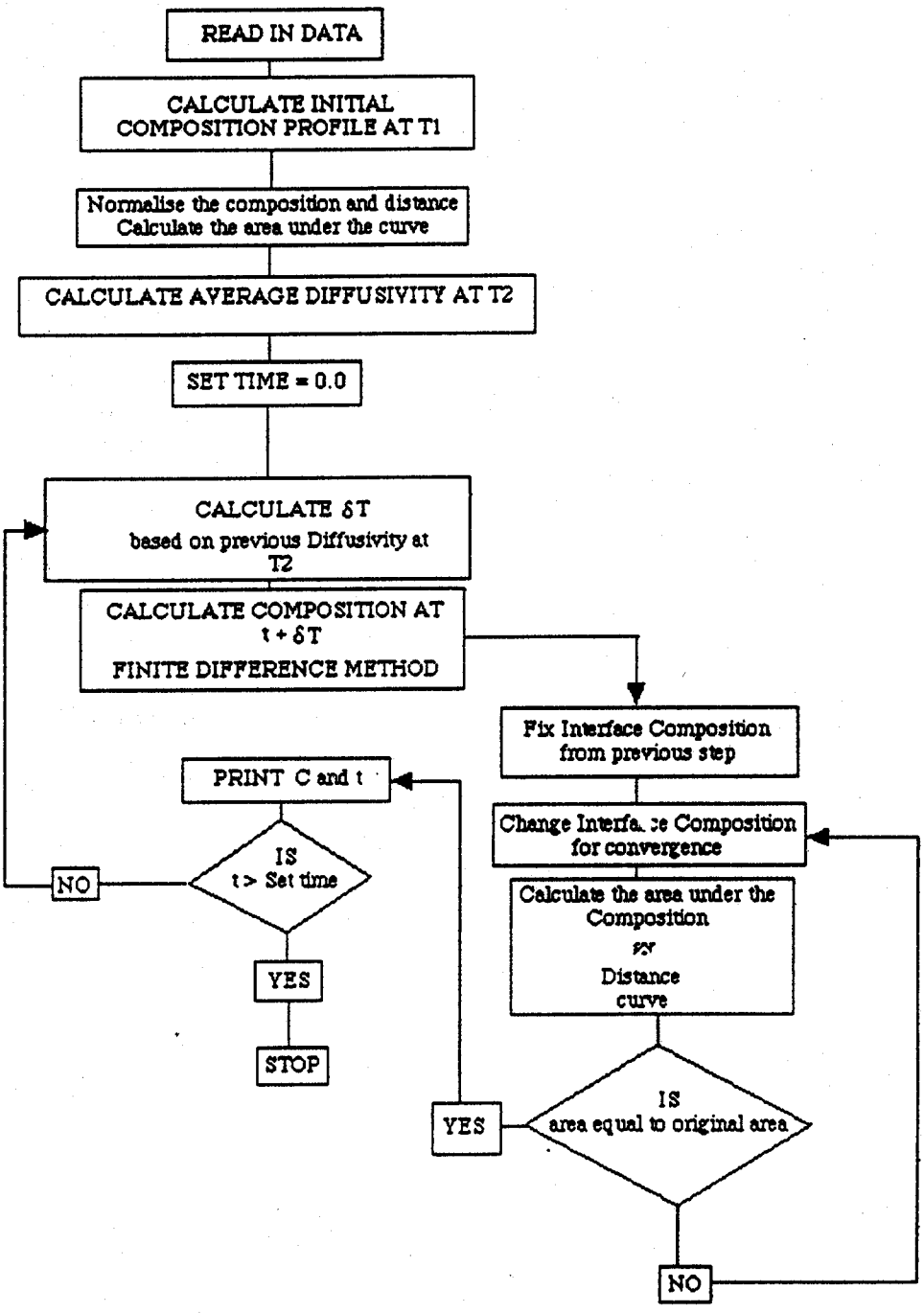

Fig. 4.18 Flow Chart indicating the finite difference method for simulating the cascade of interface composition with time.

Chapter 5

Mechanism of the Transition from Bainite to Acicular Ferrite

5.1 Introduction

Acicular ferrite is also found in wrought steels which have deliberately been inoculated with nonmetallic inclusions (Imagumbai *et al.*, 1985, Yamamoto *et al.*, 1987, Nishioka *et al.*, 1988). Present and previous experimental data have provided convincing evidence that acicular ferrite is essentially intragranularly nucleated bainite (Yang and Bhadeshia 1987a, Strangwood and Bhadeshia, 1987a, Sugden and Bhadeshia, 1989b). Some of the experimental results which confirm that acicular ferrite is nothing but intragranularly nucleated bainite were summarised schematically in Fig. 4.13. The transformation temperatures are identical for all the cases illustrated, the differences being that: (Fig. 4.13a) inclusion density changed for the same austenite grain size (Harrison and Farrar, 1981); (Fig. 4.13b) an increase in the austenite grain size at constant inclusion density stimulates a transition from a predominantly bainitic to an acicular ferrite microstructure (Yang and Bhadeshia, 1987a); (Fig. 4.13c) the growth of a layer of inert allotriomorphic ferrite at the austenite grain surfaces causes a transition from bainite to acicular ferrite (chapter 4). Henceforth, *active* allotriomorphic ferrite is defined as that which is able to develop into other transformation products such as Widmanstätten ferrite or bainite at the transformation temperature of interest. The allotriomorphic ferrite is said to be *inert* when the local reduction in transformation temperature at the ferrite/austenite interface due to the partitioning of carbon prevents the development of secondary Widmanstätten ferrite or bainite. The present chapter describes experiments to investigate this mechanism.

5.2 Method & Experimental Techniques

To enable the acicular ferrite/bainite transition to be studied easily, it is necessary that the steel used should contain a substantial quantity of nonmetallic inclusions of the type responsible for the nucleation of acicular ferrite. Consequently, steel samples machined from alloy 77 were used in this study. The composition is presented in Table 2.2. The sample preparation procedures were similar to the method described in chapter 2. Subsequent heat-treatments were conducted in a *Theta Industries* high-speed dilatometer with a helium gas-quench facility. The austenitisation treatment was carried out under helium in the dilatometer chamber. The prior austenite grain size generated by austenitising at 1150°C for 10 minutes was found to be about 70 μm (mean lineal intercept). Regular optical and transmission electron micrography was carried out.

Details of the dilatometric technique have been described previously; the interpretation of such data requires a knowledge of lattice parameters and thermal expansivities of the phases involved. The lattice parameter of ferrite was measured using X-ray diffraction (Debye-Scherrer, Cu-K_α, 45 kV). With a Nelson-Riley extrapolation of the measured data, the accurate ferrite lattice parameter was found to be 0.28739 ± 0.00024 nm. For austenite, the lattice parameter can be estimated using published data (Dyson and Holmes, 1970 and Bhadeshia, 1982b). The thermal expansion coefficients of austenite and ferrite were measured dilatometrically to be $1.9955 \times 10^{-5} \pm 0.2 \times 10^{-7}\,K^{-1}$ and $1.3941 \times 10^{-5} \pm 0.2 \times 10^{-7}\,K^{-1}$ respectively.

5.3 Results & Discussion

5.3.1 Heat-Treatment

Figure 5.1 illustrates the calculated time-temperature-transformation (TTT) diagram for the alloy using the procedures developed by Bhadeshia (1982a). If thin layers of allotriomorphic ferrite (α) are to be utilised in order to prevent austenite (γ) grain boundary nucleated reactions from stifling the development of intragranularly nucleated acicular ferrite, then the allotriomorphic ferrite itself must be inert. It is well known, however, that Widmanstätten ferrite packets or bainite sheaves are often seen to grow from α/γ interfaces, especially when the α has an orientation with the austenite which is in the Bain region (Crosky *et al.*, 1980). In other circumstances, the ferrite appears unable to develop into other transformation products (chapter 4). A major purpose of this work was to investigate whether it is the carbon diffusion field established at a temperature T_α in front of the allotriomorphic ferrite/austenite interface that sometimes prevents the ferrite from developing into Widmanstätten ferrite or bainite during subsequent transformation at a lower temperature T_b.

A series of experiments was designed to investigate the role of the partitioned carbon (Fig. 5.2, Table 5.1); the detailed choice of transformation temperatures for these experiments is discussed later:

(a) Heat-treatment H1 involved a low allotriomorphic ferrite transformation temperature (T_α), in order to render it inert (a low T_α corresponds to a large value of $x^{\gamma\alpha}$, the carbon concentration in the austenite at the austenite/ferrite interface).

(b) As a control experiment, H2 was designed with a high T_α, such that the allotriomorphic ferrite would be active on subsequent transformation at T_b.

(c) Any carbon build up at the α/γ interface can in principle be homogenised by annealing at a high temperature $T_a > T_\alpha$. This could render initially inert allotriomorphic ferrite active. Heat-treatments H3 and H4 were designed to test this idea.

(d) In heat-treatment H5, the temperature T_b was deliberately set to be larger than the

bainite–start temperature of the alloy, in order to confirm that acicular ferrite, which is supposed to be intragranularly nucleated bainite, does not form.

Table 5.1 Heat–treatment schedules. The samples were austenitised at 1150 °C for 10 minutes prior to transformation at lower temperatures. The temperatures (T) are all stated in °C, and the corresponding time periods (t) in minutes. The samples were all quenched after the final isothermal reaction. T_α is the allotriomorphic ferrite growth temperature, T_a is an annealing temperature and T_b is a bainitic transformation temperature.

	T_α	t_α	T_a	t_a	T_b	t_b
H1	660	1.0	–	–	501	5
H2	740	4.0	–	–	500	60
H3	660	1.0	760	0.5	500	60
H4	660	1.0	750	1.0	500	60
H5	660	1.0	–	–	600	1

The temperatures for the heat–treatments just described were determined theoretically, by calculating the Widmanstätten ferrite–start and bainite–start temperatures for the austenite (of composition $x^{\gamma\alpha}$) adjacent to the allotriomorphic ferrite, as illustrated in Fig. 5.3. In Fig. 5.3, the horizontal axis represents the temperature at which allotriomorphic ferrite grows, whereas the vertical axis represents the Widmanstätten ferrite–start or bainite–start temperature of the austenite at the allotriomorphic ferrite/austenite interface. The method for thermodynamic and transformation–start calculations have been described before (chapter 1). It is clear from Fig. 5.3 that for T_α = 660°C, the allotriomorphic ferrite is expected to be inert when T_b = 500°C. For the same value of T_b = 500°C, allotriomorphic ferrite generated by transformation at $T_\alpha > 720$°C is expected to be active.

These calculations are valid for heat–treatments H1 and H2, which do not include any intermediate annealing treatment at T_a. They assume therefore that any carbon concentration built up in the austenite as the allotriomorph grows, is retained as the sample is cooled rapidly to T_b. On the other hand, samples H3 & H4 were annealed at T_a immediately after the growth of allotriomorphic ferrite and before heat–treatment at T_b. It is therefore necessary to model any change in the carbon concentration profile ahead of the α/γ interface during the annealing treatment.

The distribution of carbon (x) in front of a ferrite allotriomorph of half–thickness Z in the absence of soft–impingement is given by Coates (1973b).

$$x\{X,t\} = \overline{x} + (x^{\gamma\alpha} - \overline{x})\left[\frac{1 - \mathrm{erf}\{X/(4\underline{D}t)^{0.5}\}}{1 - \mathrm{erf}\{Z/(4\underline{D}t)^{0.5}\}}\right] \tag{5.1}$$

where X is the distance in the austenite ahead of the interface, and $\overline{x}$ is the average carbon concentration of the steel. $\underline{D}$ is the weighted average carbon diffusivity in austenite (Trivedi and Pound, 1967):

$$\underline{D} = \int_{x^{\gamma\alpha}}^{\overline{x}} D\{x\}/(\overline{x} - x^{\gamma\alpha}) \tag{5.2}$$

where D is the concentration dependent diffusion coefficient of carbon in austenite, calculated as in Siller and Mclellan (1969,1970).

Having calculated this carbon concentration profile generated at T_α, a finite difference method described in chapter 4 was utilised to see how it homogenises during heat–treatment at T_a (Fig. 5.4). The concentration at the ferrite/austenite boundary after the annealing treatment is therefore known, permitting the calculation of Widmanstätten ferrite–start and bainite–start temperatures at that location. With the help of such calculations, it was possible to demonstrate (Table 5.2) that heat–treatments H3 and H4, both of which incorporate an intermediate anneal at T_a, should activate the ferrite which would otherwise be inert. The ferrite half–thickness values necessary for the calculations were measured directly using optical microscopy to be around 3.5 μm. This probably overestimates the thickness due to sectioning errors. The calculations nevertheless demonstrated that even with any overestimated thickness, the annealing treatment is more than adequate in activating the ferrite.

Fig. 5.5 shows the microstructure of a sample which was quenched directly from the austenitisation temperature to another temperature (500 °C) below B_S. The experiment confirms that in ordinary circumstances, heterogeneous nucleation at the austenite grain surfaces dominates the transformation behaviour, leading to a fully bainitic microstructure rather than one containing intragranularly nucleated bainite (*i.e.*, acicular ferrite). This is in complete contrast with the microstructure obtained during heat–treatment H1 (Fig. 5.6), in which the first transformation product to form is allotriomorphic ferrite, which completely decorates the austenite grain surfaces. Since this allotriomorphic ferrite is inert (Table 5.2), transformation at T_b leads to the formation of acicular ferrite.

Figure 5.7 (heat–treatment H2) shows a case where the allotriomorphic ferrite is ineffective. Because it formed at a relatively higher temperature, $x^{\gamma\alpha}_{T_a}$ is small enough to permit the ferrite to develop into bainite during transformation at T_b. There is clear evidence of the growth of bainite sheaves from the allotriomorphic ferrite (which is therefore classified to be active, Table 5.2); consistent with theory, bainite is obtained instead of acicular ferrite.

Table 5.2 The results of calculations designed to indicate whether the allotriomorphic ferrite generated in heat-treatments H1–H4 should be inert or active. $x_{T_a}^{\gamma\alpha}$ is the carbon concentration in the austenite at the α/γ interface at the temperature T_α. $x_{T_a}^{\gamma\alpha}$ is the carbon concentration in the austenite at the α/γ after heat-treatment at T_a. Since T_b = 500°C, $x_{T_a}^{\gamma\alpha}$ must be less than 0.011 mole fraction if the ferrite is to be active during isothermal holding at T_b. The microstructure observed experimentally (within the austenite grains) is listed in the last column. The concentrations are all in mole fractions, the temperatures in °C and time in minutes.

	T_α	t_α	$x_{T_a}^{\gamma\alpha}$	T_a	t_a	$x_{T_a}^{\gamma\alpha}$	micro-structure
H1	660	1	0.0274	501	5	0.0224	acicular
H2	740	4	0.0086	500	60	0.0079	bainite
H3	660	1	0.0274	760	0.5	0.0119	bainite
H4	660	1	0.0274	750	1.0	0.0092	bainite

Experiments H3 and H4 both show bainitic microstructures (Fig. 5.8a,b), because in both cases, the annealing treatment at T_a leads to a reduction in the concentration of carbon at the α/γ interface, rendering the allotriomorphic ferrite active.

Fig. 5.9 confirms that acicular ferrite will not form if T_b is greater than the bainite–start temperature of the alloy, even when the austenite grain boundaries are covered with layers of inert allotriomorphic ferrite. Heat-treatment H5 has a microstructure of just allotriomorphic ferrite and the martensite obtained on quenching to ambient temperature.

5.3.2 Interpretation of dilatometric data

The dilatometric technique can be extremely useful in studying transformations because it allows the transformation to be followed as it happens (Fig. 5.10). The three typical examples presented in Fig. 5.10 illustrate direct transformation to bainite, a two–stage heat–treatment involving first the formation of allotriomorphic ferrite and then acicular ferrite, and finally, a three–stage heat–treatment in which the sample is annealed at an elevated temperature after the growth of allotriomorphic ferrite. It is particularly notable that in the latter case, no transformation occurs during annealing at T_a, although the distribution of carbon must homogenise as discussed earlier. This is because the paraequilibrium fraction of ferrite at T_a is approximately that which was induced to form at T_α.

Figure 5.11a illustrates the length change observed during isothermal transformation at 660°C; the incubation time prior to the onset of substantial reaction is about 10 s, which is

consistent with the calculated TTT diagram presented in Fig. 5.1. Fig. 5.11b shows the how the isothermal transformation at temperatures below B_S ceases, so that the carbon concentration of the residual austenite at that stage can be compared against the T_o' curve (discussed later) in order to deduce the mechanism of transformation.

The dilatometric data can be interpreted further, since the length changes can be converted into the volume fraction of transformation using the lattice parameter and thermal expansivity measurements presented earlier (Bhadeshia, 1982b, chapter 2 and 4). The volume fraction data can in turn be combined with a conservation of mass criterion to estimate the carbon concentration of the residual austenite at any stage of reaction. It is interesting to see that for heat–treatments H1 and H4, the formation of acicular ferrite and bainite (respectively) ceases as the carbon concentration of the residual austenite reaches the T_o' curve of the phase diagram (Fig. 5.12). This curve defines the locus of all points on the phase diagram at which austenite and strained–ferrite of the same composition have the same free energy (see for example, Bhadeshia and Christian, 1990). If that carbon concentration is exceeded, then transformation cannot proceed without the partitioning of carbon. Bainite and acicular ferrite are both known to stop growing when the T_o' curve is reached, indicating the existence of an *incomplete reaction phenomenon* which can be interpreted to indicate that bainite and acicular ferrite grow without diffusion, any partitioning of carbon occurring after the growth event. These results are therefore significant in two respects; firstly, acicular ferrite is once again confirmed to have the same mechanism of transformation as bainite, in agreement with previous results. The second point is that the enrichment of austenite caused by the initial partial transformation to allotriomorphic ferrite also contributes to an early cessation of transformation to bainite or acicular ferrite.

5.4 Conclusions

The formation of acicular ferrite in steels containing intragranular nucleation sites can be enhanced by reducing the number density of austenite grain boundary nucleation sites. This can be done by decorating the austenite grain surfaces with thin layers of allotriomorphic ferrite. The ferrite must however, be inert in the sense that it should not develop at lower transformation temperatures into secondary Widmanstätten ferrite or bainite. It can be rendered inert by the the partitioning of carbon into the austenite at the ferrite/austenite interface, as long as the local concentration is large enough to depress the local Widmanstätten ferrite–start or bainite–start temperature below the actual heat–treatment temperature. Finally, the results are all consistent with the hypothesis that acicular ferrite is nothing but intragranularly nucleated bainite.

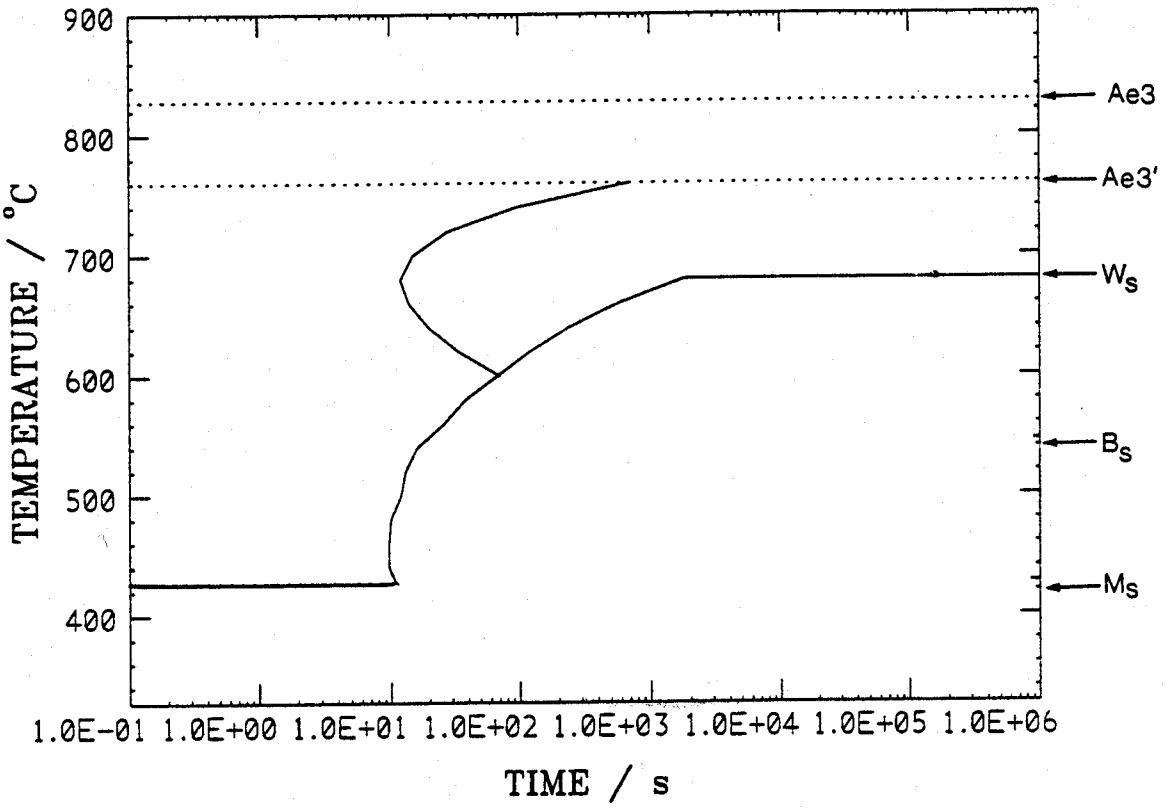

Fig. 5.1 Calculated time–temperature–transformation diagram for the alloy studied. The thermodynamically calculated transformation temperatures (°C) are $M_S = 427$, $B_S = 546$, $W_S = 680$, $Ae_3' = 760$ and $Ae_3 = 828$ representing the martensite–start, bainite–start, Widmanstätten ferrite–start, paraequilibrium $\gamma/(\gamma+\alpha)$ temperature and equilibrium $\gamma/(\gamma+\alpha)$ temperature respectively.

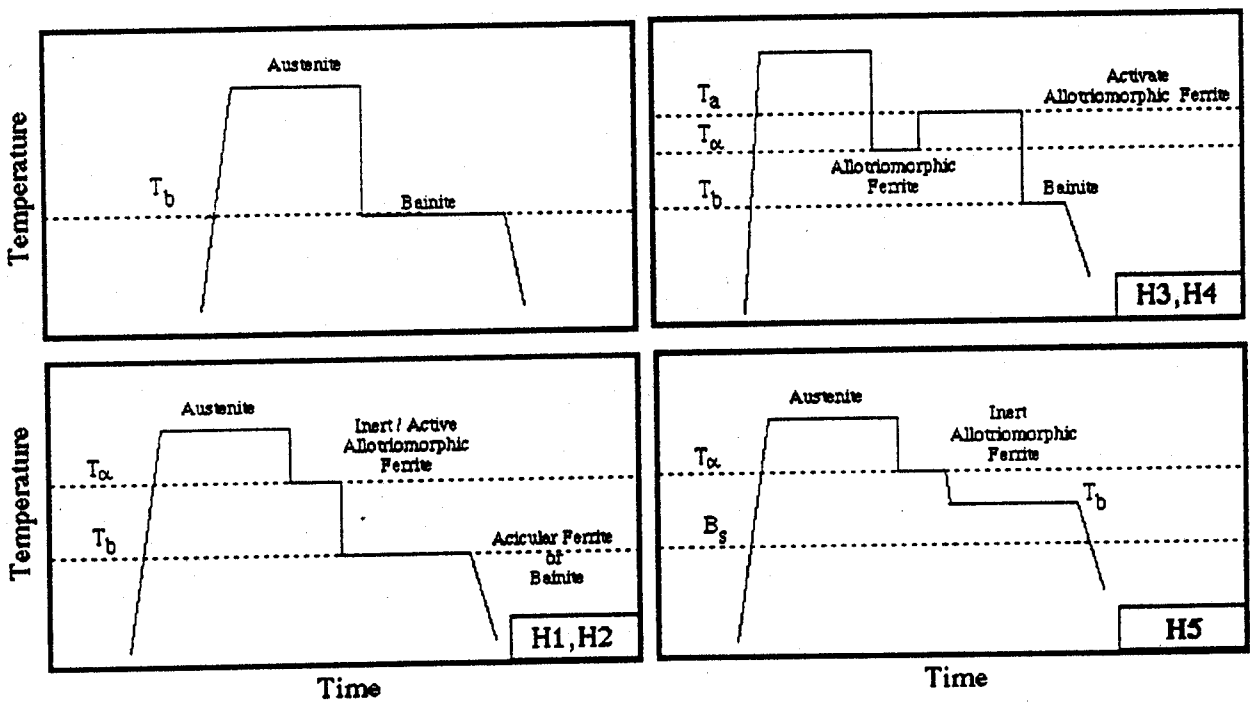

Fig. 5.2 Schematic illustration of the heat-treatments used.

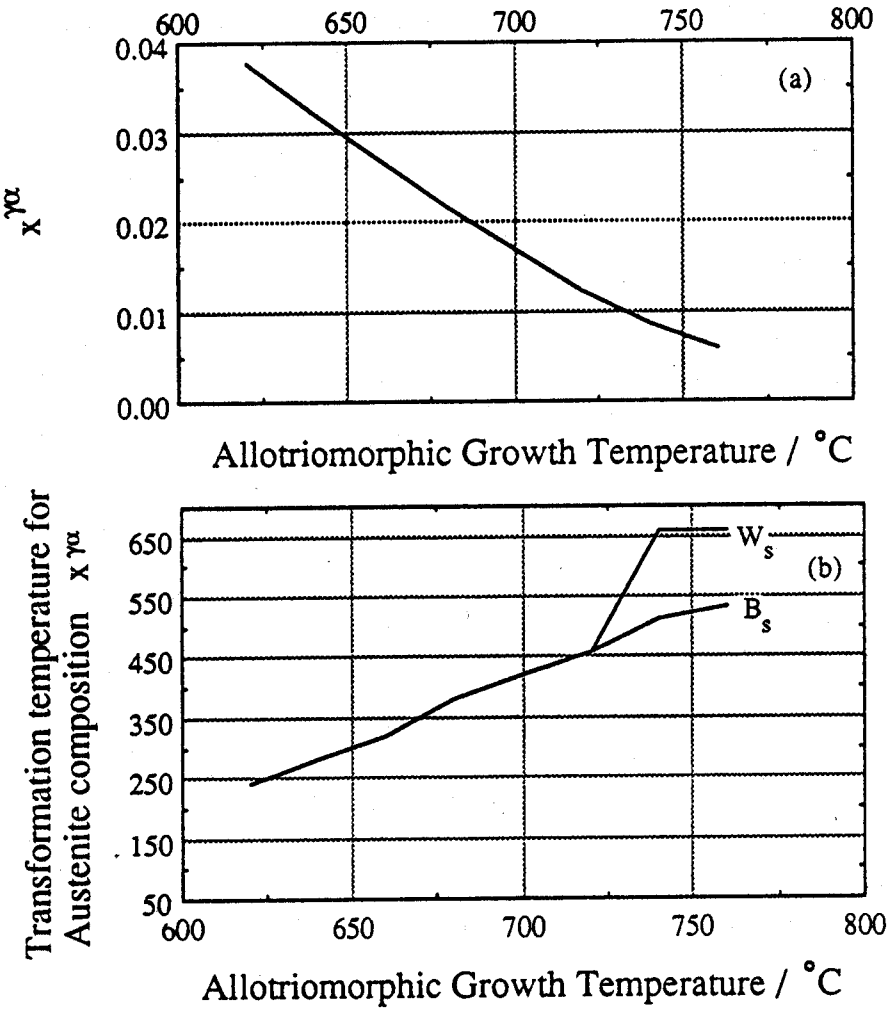

Fig. 5.3 Calculations designed to predict whether the allotriomorphic ferrite should be inert or active. (a) Variation of $x^{\gamma\alpha}$ as a function of the temperature at which allotriomorphic ferrite grows. (b) The horizontal axis represents the temperature at which allotriomorphic ferrite is induced to form. The vertical axis represents the Widmanstätten ferrite–start or bainite–start temperature of the austenite at the allotriomorphic ferrite/austenite interface.

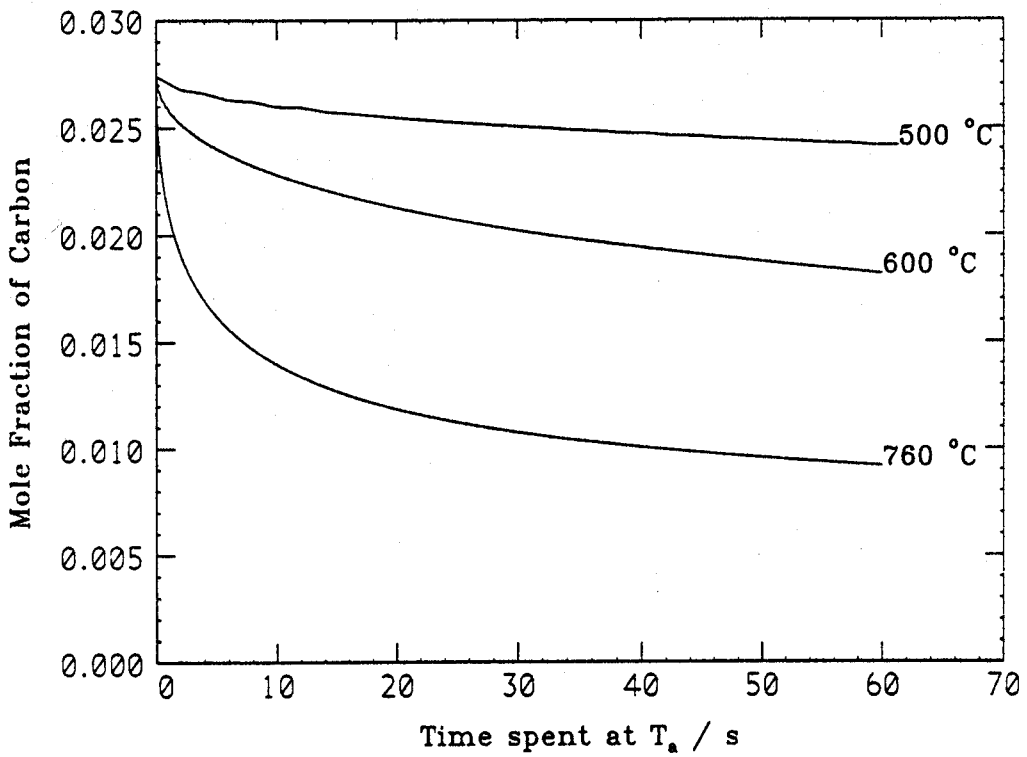

Fig. 5.4 Finite–difference modelling of the homogenisation of the carbon concentration profile generated during the growth of allotriomorphic ferrite. The figure shows variation of $x^{\gamma\alpha}$ as a function of time at a given ageing temperature T_a. Notice that the ageing heat–treatment at 500 °C (the temperature at which bainite or acicular ferrite are formed) hardly reduces the $x^{\gamma\alpha}$, in comparison to heat–treatment at 760 °C.

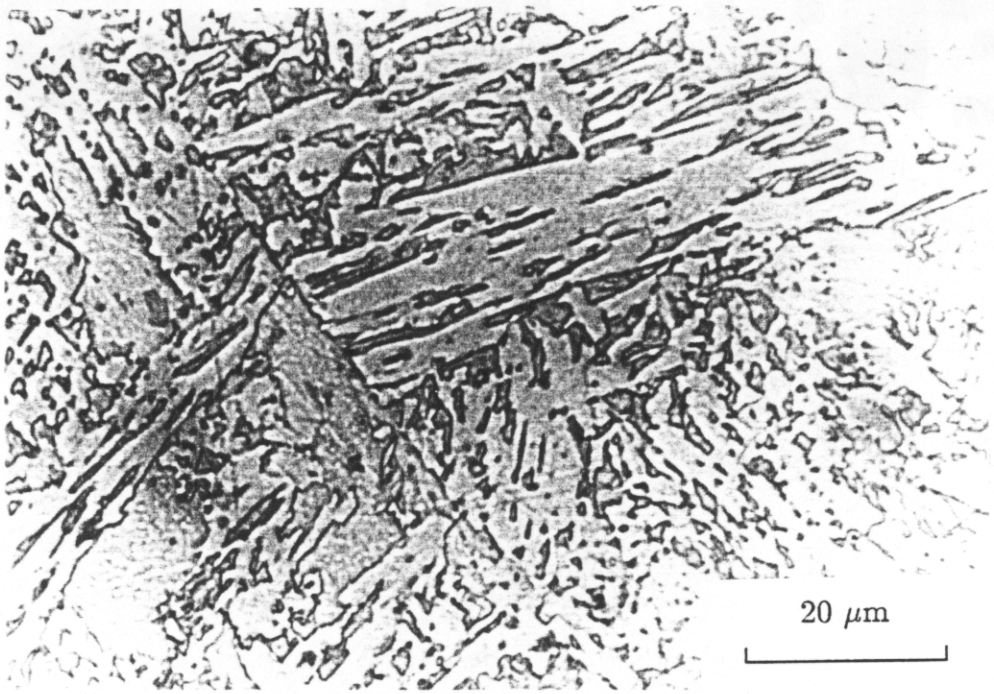

Fig. 5.5 The bainitic microstructure generated during isothermal transformation at 500 °C for 60 minutes followed by quenching to ambient temperature.

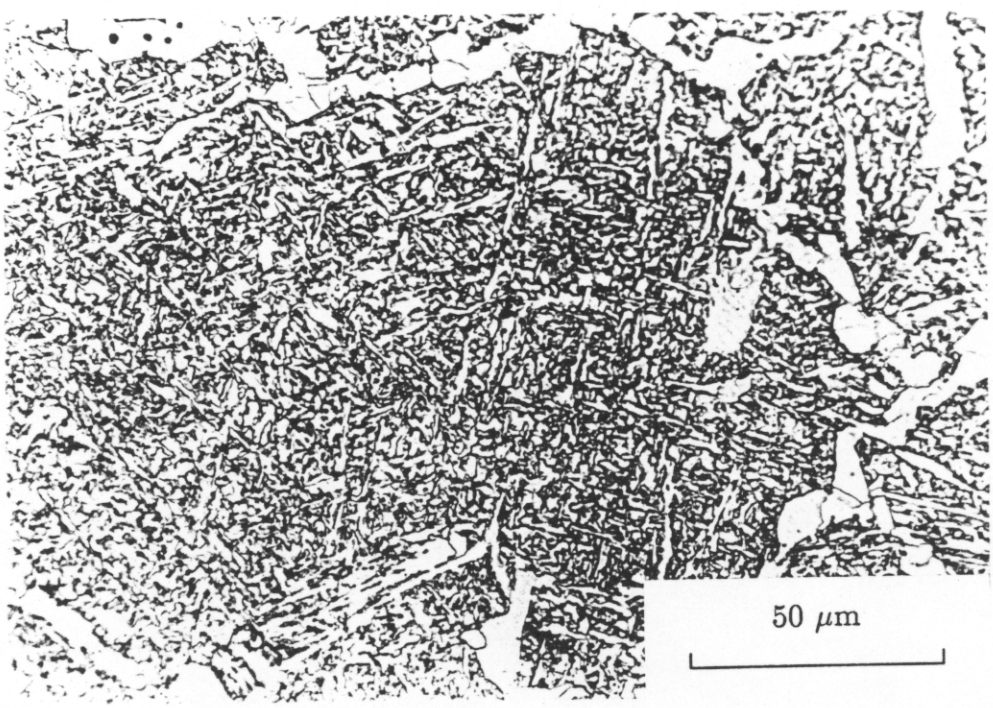

Fig. 5.6 The microstructure generated by heat-treatment H1. The allotriomorphic ferrite layer is inert, giving acicular ferrite in the interiors of the austenite grains.

(a)

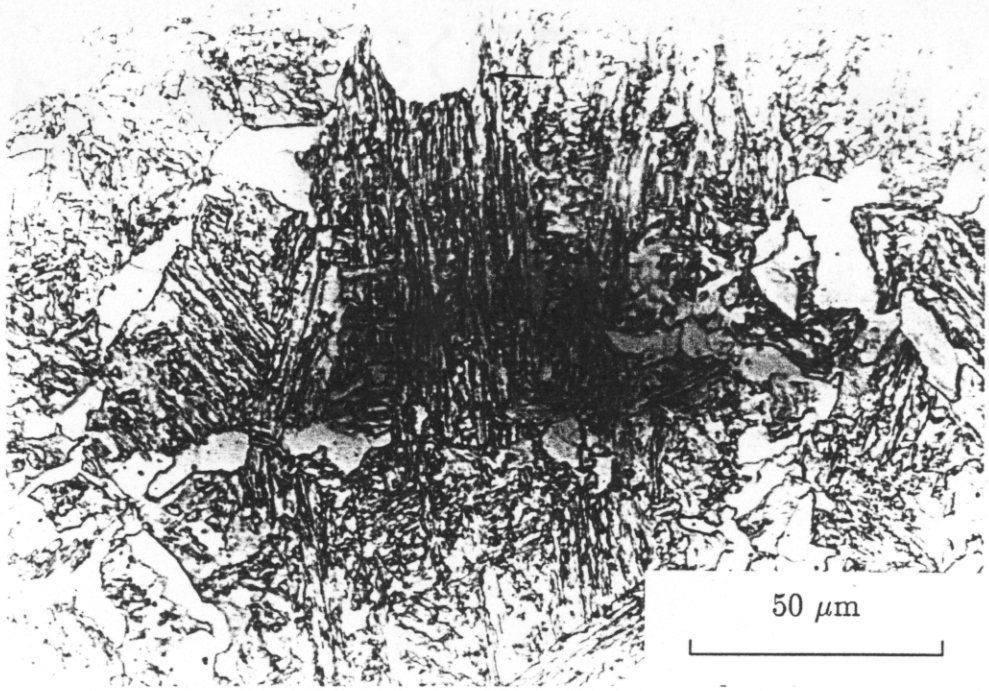

(b)

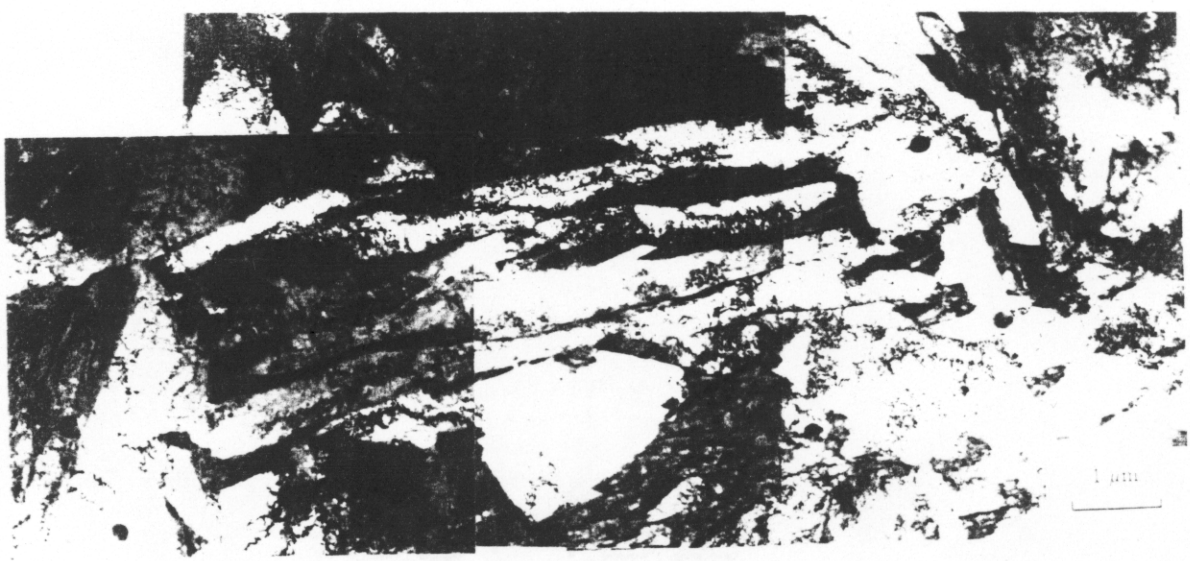

Fig. 5.7 The microstructure generated by heat–treatment H2, in which the allotriomorphic ferrite is active, with bainite sheaves in the middle of the austenite grains:

(a) optical micrograph,

(b) thin foil transmission electron micrograph of allotriomorphic ferrite and bainite sheaf.

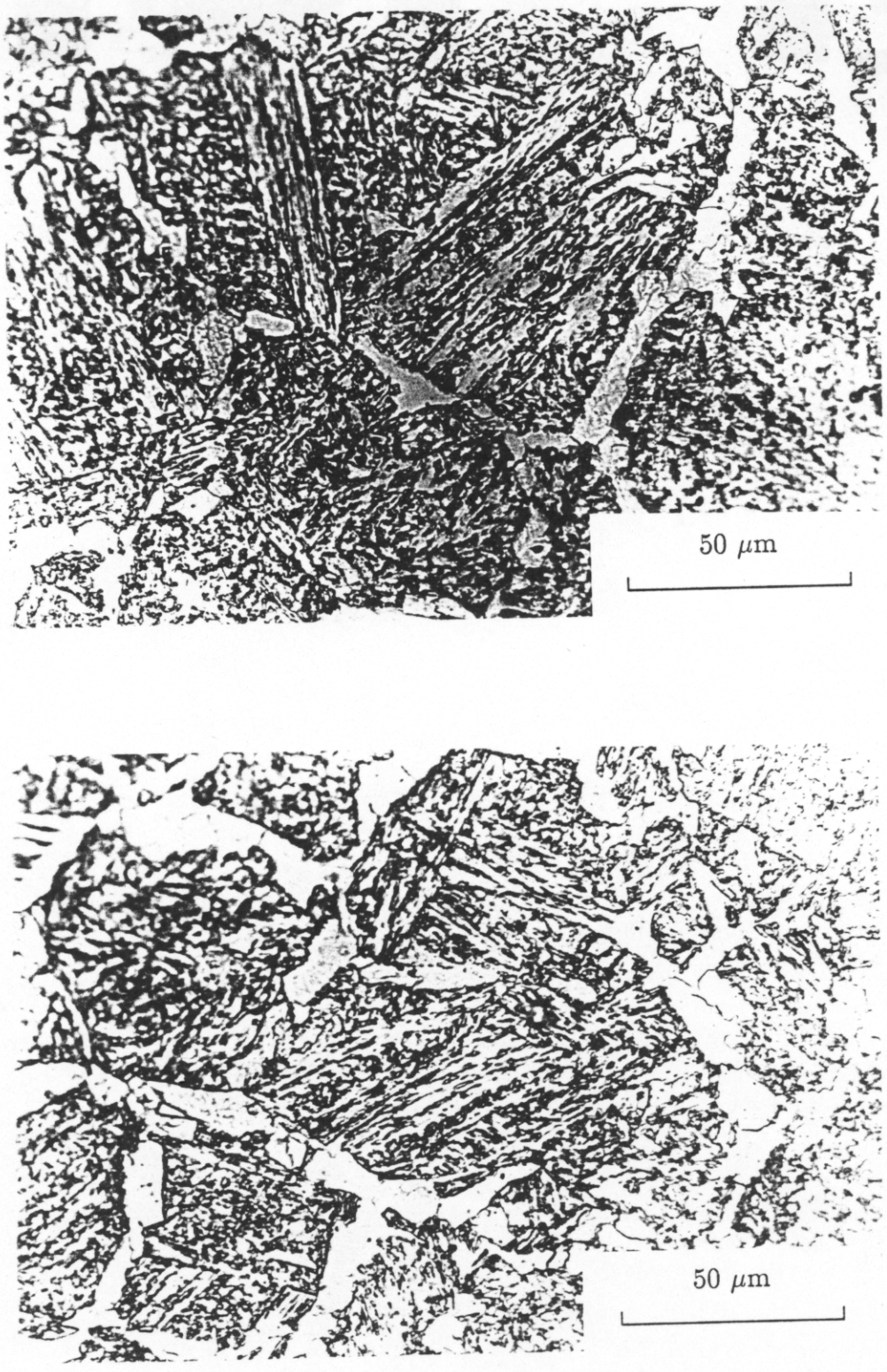

Fig. 5.8 The microstructures generated by heat-treatments H3 (a) and H4 (b), where the allotriomorphic ferrite was activated by annealing at 760 and 750 °C, respectively. Bainite sheaves have formed as a consequence.

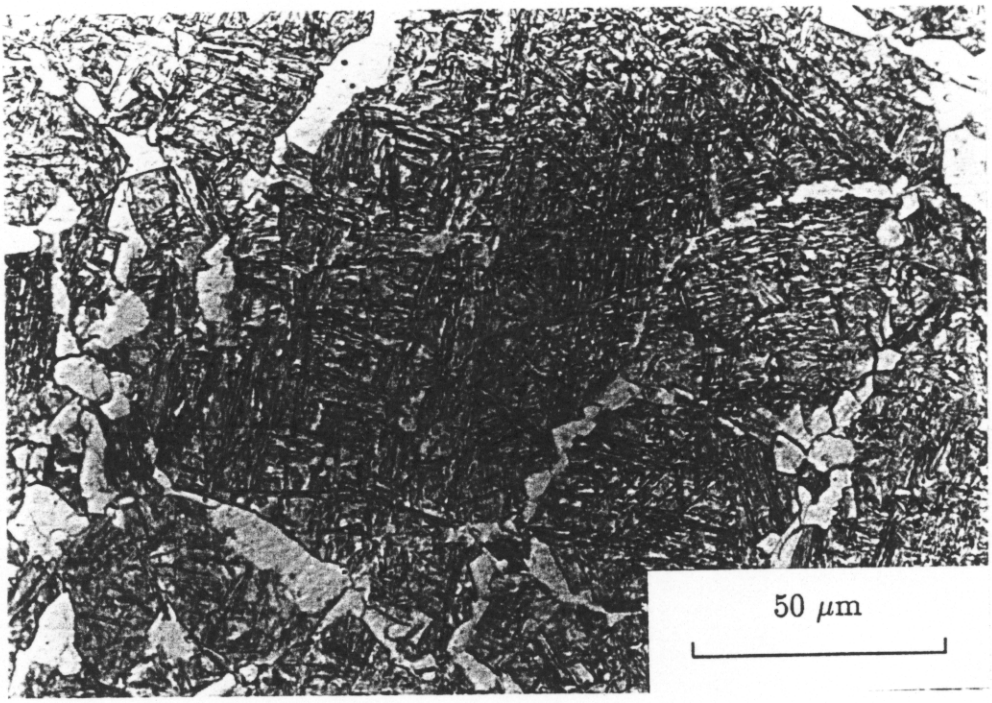

Fig. 5.9 The microstructure generated by heat-treatment H5, consisting of allotriomorphic ferrite and martensite, since isothermal holding at a temperature above B_s did not cause any transformation.